Wavefront Sensorless Adaptive Optics Swept-Source Optical Coherence Tomography at 1060nm

by

Sujin Lee

B.A.Sc. (Engineering Science), Simon Fraser University, 2015

Thesis Submitted in Partial Fulfillment of the
Requirements for the Degree of

Master of Applied Science

In the
School of Engineering Science
Faculty of Applied Sciences

SIMON FRASER UNIVERSITY

Fall 2015

Approval

Name:	**Sujin Lee**
Degree:	**Master of Applied Science**
Title:	***Wavefront Sensorless Adaptive Optics Swept-Source Optical Coherence Tomography at 1060 nm***
Examining Committee:	**Chair: Dr. Mirza Faisal Beg, P. Eng.** Professor

Dr. Marinko V. Sarunic, P. Eng.
Senior Supervisor
Associate Professor

Dr. Yifan Jian
Supervisor
University Research Associate

Dr. Stefano Bonora
External Examiner
Research Scientist
CNR - Institute of Photonics

Date Defended: Dec. 23, 2015

Abstract

Optical Coherence Tomography (OCT) has revolutionized modern ophthalmology, providing depth resolved images of the retinal layers in a system that is suited to a clinical environment. A limitation on the performance and utilization of the OCT systems has been the lateral resolution; whereas the axial resolution is a function of the light source, the lateral resolution is dependent on the delivery optics. In this thesis, a compact lens based OCT system is presented that is capable of imaging the different retinal layers at a cellular lateral resolution with the combination of wavefront sensorless adaptive optics with dual variable optical elements. The central operating imaging wavelength of the wavelength swept OCT engine was 1060nm, close to the dispersion minimum of water (and the vitreous humor in the eye). A commercially available variable focal length lens is utilized to correct for a wide range of defocus commonly found in patient's eyes, and a multi-actuator deformable lens for aberration correction to obtain near diffraction limited imaging at the retina. A parallel processing computational platform permitted real-time image acquisition and display. Cross-sectional images of the retinal layers and *en face* images of the cone photoreceptor mosaic acquired in vivo from research subjects are presented.

Keywords: high-resolution OCT; variable-focus lens; multi-actuator adaptive lens; *en face* OCT

Acknowledgements

I would like to express my sincere deepest gratitude to my senior supervisor, Dr. Marinko V. Sarunic. Ever since I became his student, he has motivated me and sought what is best for me to become a better engineer. He has provided insightful discussions about the research and there was always much to learn. I appreciate all his contributions of time, ideas, and project funding to make my research experience productive and stimulating. It has been such an honor to have him as my supervisor; I could not have imagined having a better mentor.

I would like to thank Dr. Yifan Jian for playing a supervisory role throughout my degree. I am also grateful for his advice, knowledge, and enthusiasm towards the research. Without his precious support, it would not have been possible to conduct this research. I am also thankful to Dr. Stefano Bonora. During a month of research under his guidance I have learned to be a better researcher, providing insightful suggestions.

I would like to thank Dr. Glenn Chapman and Dr. Pierre Lane for providing their immense knowledge in optics. I am thankful to Michelle Cua for guiding me in many details during my graduate degree. I also thank Dr. Myeongjin Ju for all the help he provided near the end of my degree.

I am very grateful to have been part of the Biomedical Optics Research Group (BORG). I am especially appreciated to BORG members, Daniel Wahl, Maxwell Miao, Bengt Haunderland, Morgan Heisler, Dr. Yuan Zhao, Dr. Mingyu Zhao, and Dr. Sieun Lee. I was honored to have worked with the past BORG members Lukas-Karim Merhi, Kevin Wong, and Dr. Jing Xu.

Lastly, I would like to thank my family for support, love, and encouragement during my graduate endeavor.

Table of Contents

List of Figures

List of Symbols

$\psi(r,\theta)$	Aberration Function
M_i	Modal Coefficient
$Z_i(r,\theta)$	Zernike Polynomial
r	Distance in polar coordinates
θ	Angle in radian in polar coordinates
n	Radial Order of Zernike Polynomial
m	Angular Frequency of the Zernike Polynomial Mode
R	Radial Variable
$J(\boldsymbol{k})$	Merit Function
$\boldsymbol{k}$	Zernike Coefficient Vector
$I^{w(\boldsymbol{k})}(x,y)$	Overall Intensity
λ_c	Central Wavelength
$\Delta\lambda$	Bandwidth

List of Acronyms

OCT	Optical Coherence Tomography
SS	Swept Source
cSLO	Confocal Scanning Laser Ophthalmoscopy
PSF	Point Spread Function
AO	Adaptive Optic
WFS	Wavefront Sensor
SHWFS	Shack-Hartmann Wavefront Sensor
DM	Deformable Mirror
AL	Adaptive Lens
CCD	Charge-Coupled Device
PZT	Piezoelectric
WSAO	Wavefront Sensorless Adaptive Optic
RGC	Retinal Ganglion Cell
ONH	Optic Nerve Head
ISAM	Interferometric Synthetic Aperture Microscopy
GPU	Graphic Processing Unit
FBG	Fiber-Bragg Grating
VL	Variable-Focus Lens
D	Diopter
FWHM	Full Width Half Maximum
VCSEL	Vertical Cavity Surface Emitting Laser
FDML	Fourier Domain Mode Locking
LSQLIN	Linear Least-Square
BVLS	Bounded-Variable Least Square
AMD	Age-related Macular Degeneration
SDD	Sub-Retinal Drusenoid Deposit

Chapter 1. Theoretical Concepts of Adaptive Optics

This chapter explains the role of various adaptive optics (AO) components, focusing on the deformable elements, such as a deformable mirror (DM) or an adaptive lens (AL), and the role of the wavefront sensor (WFS). It also introduces both WFS and wavefront sensorless adaptive optics (WSAO) techniques. This chapter concludes with an overview of the remainder of this thesis.

1.1. Background

Historically, AO was introduced to form sharp images of stars by correcting a wavefront error caused by atmospheric distortions [1]. It is one of the most revolutionary discoveries in astronomy, allowing astronomers to see further into space with higher resolution, and answer unexplained questions about the universe [2].

Adaptive optics has also been applied to biological imaging applications, correcting wavefront aberrations in the sample. Applied to human in vivo imaging, AO has evolved into a powerful tool in retinal imaging with the capability of observing retinal structures at the cellular level. While adaptive optical microscopy was introduced in the early 2000s, AO is now prevalent in pre-clinical diagnostic tools including the conventional fundus (flood-illumination) camera, confocal scanning laser ophthalmoscopy (cSLO), and optical coherence tomography (OCT) [3]–[6]. Retinal images can be acquired by illuminating a light source into the eye and measuring the intensity of the back reflected signal. Similar to wavefront distortions created by atmospheric turbulence, the human eye creates chromatic, longitudinal, and transverse aberrations [7]. Integrating AO into retinal imaging modalities significantly improves image quality of features that are unresolvable or hard-to-resolve with conventional imaging techniques.

1.2. Image Formation

One of the main factors that determine the lateral and axial image

resolution is the point spread function (PSF). The PSF is an impulse response of a focused light source at an image's single object point. Hence, the quality of the focal spot can characterize the optical system completely [8]. When imaging the human eye with a light source, the cornea can be modeled as an ideal single thin lens system. Illuminating an ideal focusing lens with a uniform plane wave creates a converging wave without aberrations. However, in real life scenarios, light gets distorted from its ideal form due to various sources such as lens imperfections. In this respect, AO comes into effect by correcting the aberrations, recovering optimal, diffraction limited imaging.

1.3. Aberrations

To deliver optimal performance and a diffraction limited system for human retinal imaging, it is essential to understand the nature of aberrations. An aberration is a distortion of wavefronts when rays of light do not follow the characteristics of perfect optical systems. In human eyes, the aberrations, or phase variations across the pupil, are present due to imperfect corneal shapes, an off-centered axis of the beam, or changes in the focal plane that are induced by accommodation.

In theory, the overall aberrations can be corrected by applying an equal but opposite phase aberration of the pupil. In the presence of circular pupils, Zernike polynomial functions are commonly used to mathematically describe the aberrations. The Zernike polynomials are a set of orthogonal basis functions define on the unit circle, meaning that any wavefront distortion can be modeled by an appropriate weighted sum of Zernike polynomials, much like sine and cosine functions are used in Fourier series expansions. The low-order Zernike modes correspond to classical aberration terms such as defocus, astigmatism, coma, or spherical aberration [9]–[11]. The aberration function, $\psi(x, y)$, can be expressed as the following equation:

$$\psi(r, \theta) = \sum_{i=1}^{\infty} M_i Z_i(r, \theta) \qquad \textbf{Equation 1.1}$$

where the modal coefficient M_i, describes the amplitude of each Zernike polynomial, $Z_i(r, \theta)$, that is defined over the unit circle with a set of orthogonal

functions [10]. The Zernike modes are characterized using the following definition:

$$Z_n^m(r,\theta) = \begin{cases} m < 0 : \sqrt{2} R_n^{-m}(r)\sin(-m\theta) \\ m = 0 : 0 \\ m > 0 : \sqrt{2} R_n^m(r)\cos(m\theta) \end{cases} \quad \textbf{Equation 1.2}$$

$$R_n^m(r) = \sqrt{n+1} \sum_{s=0}^{(n-m)/2} \frac{(-1)^s (n-s)!}{s!\left(\frac{n+m}{2}-s\right)!\left(\frac{n-m}{2}-s\right)!} r^{n-2s} \quad \textbf{Equation 1.3}$$

where *n*, *m*, and *R* represents radial order, angular frequency, and radial variable, respectively. The variables *n* and *m* are restricted with $n - |m|$ being even and non-negative [8].

Zernike polynomials with $m > 0$ are considered to be even functions because of their symmetry, and on the contrary, the polynomials with $m < 0$ are treated as odd functions. Each function has a unique property where an addition of two equal and opposite odd functions sums up to zero while adding two even functions doubles the amplitudes.

Index			Aberration Term
i	n	m	
0	0	0	Piston
1	1	1	Tip
2	1	-1	Tilt
3	2	0	Defocus
4	2	2	Astigmatism1
5	2	-2	Astigmatism2
6	3	1	Coma1
7	3	-1	Coma2
8	3	3	Trefoil1
9	3	-3	Trefoil2
10	4	0	Spherical
11	4	2	2nd Coma1
12	4	-2	2nd Coma2
13	4	4	2nd Astig1
14	4	-4	2nd Astig2

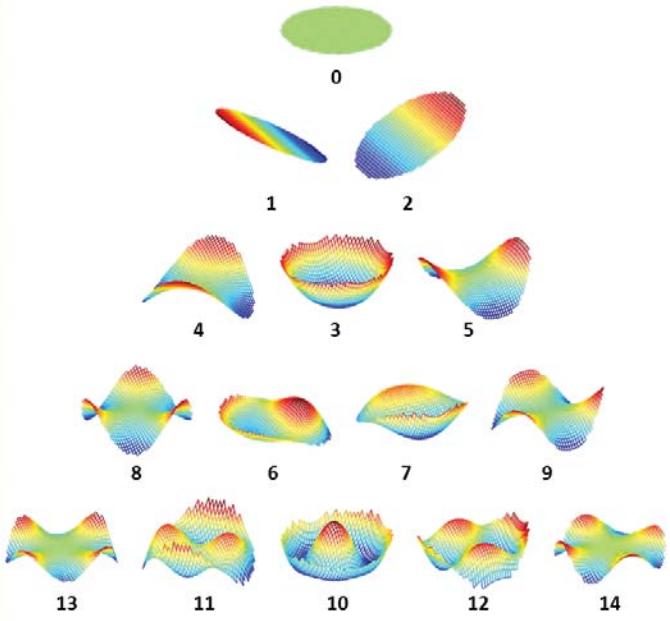

Figure 1-1: Up to 4th order of the Zernike circle polynomials are shown where numbers below each polynomial matches to the index number on the left table.

1.4. Shack-Hartmann Wavefront Sensor and Deformable Mirror

Adaptive optics is generally composed of a Shack-Hartmann wavefront sensor (SHWFS) to give feedback of perturbed wavefronts, and a DM to physically change the optical path in order to compensate for system and sample aberrations. Similarly, a spatial light modulator can be used instead of the DM to correct aberrations by adjusting the phase. Figure 1-2a shows a simple diagram of an AO system where an image is reflected by a DM and projected onto a SHWFS consisting of a high-resolution camera lenslet array – a bundle of equally spaced, small identical lenses. Aberrated wavefronts are detected by the SHWFS that is located at a conjugate plane of the image and the DM. Each sub-lens of the lenslet array takes a small part of the image and projects it onto the arrayed detector (usually a charge-coupled device (CCD) or CMOS sensor). In the presence of plane waves, the focused spot created by each lenslet will be formed in a grid characterized by the lenslet array geometry shown in Figure 1-2b. Once the wavefronts are distorted, they will create displacements in each sub-aperture image that is directly related to the approaching angle at the CCD. The converted angle measurements are fed into the DM to correct the distortion. The controlling voltage signal is generated depending on the two main types of the DM – segmented and continuous mirrors.

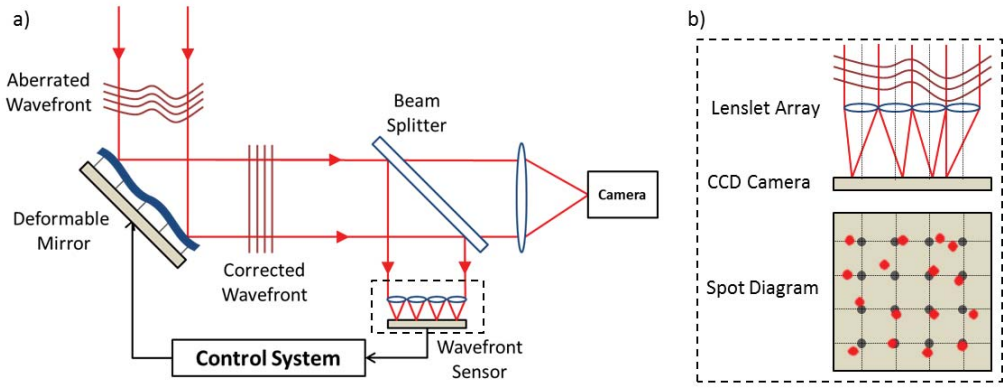

Figure 1-2: a) A simple adaptive optics schematic; b) A simple model of a Shack-Hartmann wavefront sensor; gray dots in the spot diagram are ideal results of a perfect optical system whereas red dots are distorted due to system aberrations.

The segmented DM is made up of a collection of small mirrors which are individually controlled by their own actuator using tip, tilt, and piston motions. Having each mirror isolated from its neighbors can be advantageous over a continuous DM. The segmented DM often has a smaller stroke, where a stroke is a measure of maximum actuator deflection, and may be better suited for adjusting higher order modes. The disadvantage, however, is that it encounters diffraction effects at each edge of the mirror segments.

The continuous DM consists of a thin sheet of reflector with actuators underneath, which are controlled separately but are not fully isolated due to an influence function. The function determines the effect in the overall sheet of reflector when an actuator is changed. An alternative to the actuators is a bimorph [12], which reacts by applying voltages to two different bonded metal strips.

In cases where DMs are utilized with actuators, relating each actuator to each element of sub-aperture image offsets observed with a SHWFS, the DM can contort into an equal and opposite shape of the aberrated wavefront to achieve plane wavefronts in a perfect optical system. Moreover, this correction process can be done in real time to compensate for time-varying aberrations

The deformable optical element is an essential component in high resolution retinal imaging systems. However, the relatively large size of currently available DMs requires a larger magnification at the conjugate pupil plane, which increases the overall length of the optical system. Additionally, in order to place the DM into an existing optical setup, extra space is required for the beam to be relayed and folded so that the DM can be placed in conjunction with a sample.

1.5. Adaptive Lens based Adaptive Optics

Similar to the DM introduced in section 1.4, another type of deformable element is an adaptive lens (AL), which shares similar characteristics as a continuous DM, but is transmissive rather than reflective. The AL can be designed and controlled in various ways. One particular

method is a multi-actuator adaptive lens (MAL) reported by Bonora et al. [13], as illustrated in Figure 1-3. Within two glass covers, mineral oil is enclosed with two piezoelectric (PZT) actuator rings attached to the cover and two aluminum rings, both divided into 8 equal sectors, as shown in Figure 1-3a. In each sector, the PZTs act as bimorph actuators, as mentioned in section 1.4, which control aluminum materials contained within the liquid chamber.

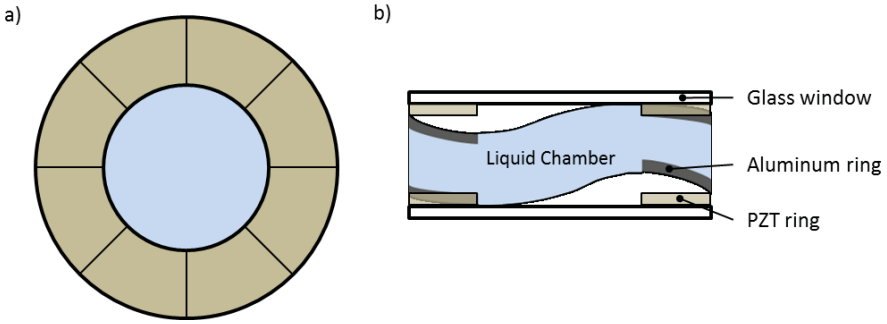

Figure 1-3: Multi-actuator adaptive lens with 8 sectors per piezoelectric actuator ring (a) and a cross section of the lens (b)

Compared to DMs, the AL has a significant advantage in the integration of AO systems into ophthalmic clinical imaging modalities. Unlike the DM based AO system, where a considerable amount of space and adjustment is required for the DM, the AL can be readily integrated in the existing optical path as long as it is placed at a conjugate plane of a sample. It may not be a seeming advantage; however, in regards to clinical imaging modalities, the size of the overall optical system is very limited. An additional feature of the AL is its capability of correcting up to 4^{th} order Zernike polynomials while optimizing an image up to its diffraction limit. A potential disadvantage of the AL is the presence of hysteresis, which is not ignorable in the AL. Nonetheless, if the lens is driven properly, it can be drastically minimized. In this thesis, the integration of the AL with a retinal imaging system was investigated.

1.6. Wavefront Sensorless Adaptive Optics

In typical retinal imaging systems, it is common for aberrations to accumulate at the cornea and inside the eye, causing distortion in wavefronts before a beam of light reaches the retina. In AO systems, the WFS receives

the aberrated wavefront and pre-deforms it using a DM or an AL, allowing it to hit the retina with an optimized beam shape. As back reflected light passes the AL, the wavefront will be reshaped to a plane wave, and is coupled into a detector.

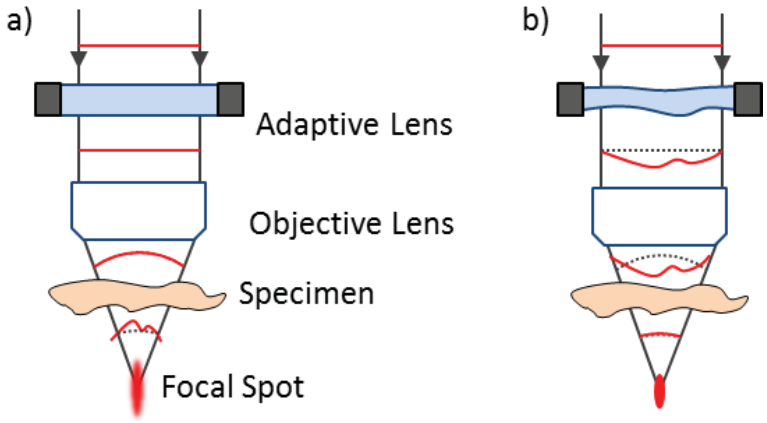

Figure 1-4: Pre-correction of aberrations caused by a specimen; a) Before the correction with AL, a wavefront got distorted before reaching a sample, generating aberrated focus; b) After pre-deforming the AL, the specimen induced aberration is removed.

One of the common elements in AO system is the SHWFS which forms a closed-loop system along with the active deformable element. However, the SHWFS is not ideal to incorporate in microscopy as a light passes an aberrative specimen twice in opposite direction, canceling odd orders and adding even orders of specimen-induced aberrations together [14]. Furthermore, the SHWFS is sensitive to back reflections, which affect the ability to accurately measure the wavefront.

For the simplicity and to avoid the double-pass aberration effect, the wavefront sensorless adaptive optics (WSAO) has been introduced. WSAO is an interative technique using the image quality to guide aberration correction, rather than a direct measurement of the wavefront aberrations. For each step of optimization, overall intensity or sharpness of an image is measured as optimizing metric. Numerous heuristics has been implemented to come up with optimization algorithms such as exhaustive search, hill-climbing algorithm, genetic algorithms, and random search [15]. Recent WSAO research has focused on optimizing a deformable element in terms of modes. Considering a

shape of an AL and cornea of a human eye, it is common to use the Zernike polynomials to optimize the AL to the opposite and equal shape of an overall ocular aberration.

The various optimization algorithms have different pros and cons, limiting the application of each. Such algorithms are characterized by its repeatability, reliability, axial resolution, and the time taken to converge to a solution [16]. Among the optimization algorithms listed above, the hill-climbing algorithm is the fastest converging algorithm, optimizing with a good repeatability, while the random search recovered the finest axial resolution but at the expense of a longer time to convergence.

For clinical use of WSAO imaging modalities, the amplitude based hill-climbing algorithm may be preferred over the alternative techniques because of its rapidness while sacrificing only slightly in performance relative to the random search algorithm. In WSAO, due to the Zernike polynomial's nature of orthogonality, the hill-climbing algorithm allows to search local maximum overall intensity at each Zernike mode individually [17]. A merit function, $J(\boldsymbol{k})$, of 2-D image can be expressed as following formula [18]:

$$J(\boldsymbol{k}) = \sum_{x,y} \left(\max\left(I^{w(\boldsymbol{k})}(x,y)\right)\right) \qquad \textbf{Equation 1.4}$$

where $\boldsymbol{k}$ is vector of the Zernike coefficients; and $I^{w(\boldsymbol{k})}(x,y)$ is the overall intensity of an image expressed in x and y coordinates. Ultimately, summing up all the individual modes using Equation 1.1 provides the optimal solution of the total ocular aberrations.

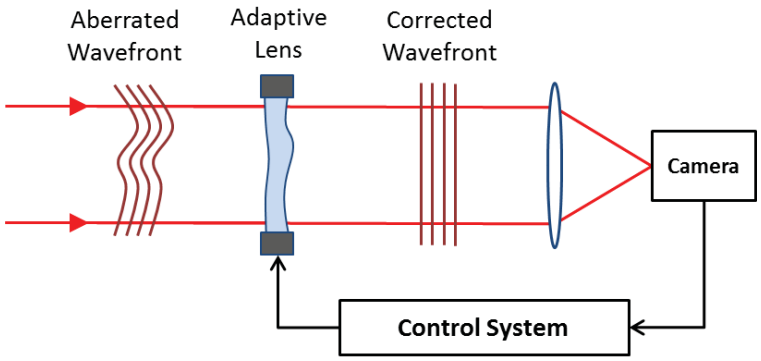

Figure 1-5: Simple WSAO schematic with an AL; A control system sweeps through each Zernike modes at different modal coefficients as it keeps the record of the most optimized coefficient at each mode.

1.7. Thesis Overview

The purpose of the research in this thesis was to investigate the design and construction of a WSAO retinal imaging system using the adaptive lens. The motivation was to develop a clinical imaging system that was compact, robust, and practical. The remainder of this thesis describes the development of a WSAO OCT for human retinal imaging. In the next Chapter, my work on developing a high speed OCT system with the basic elements of wavefront sensorless focus control is described. The performance of this imaging system was demonstrated for retinal imaging, as well as for imaging the optic nerve head, where the nerve fiber bundles exit the eye toward the brain. Chapter 3 builds on the work with the integration of the adaptive lens described in the section 1.6 that is able to correct higher order aberrations than just defocus. The thesis concludes with a description of future work, using the WSAO OCT system for clinical studies in collaboration with ophthalmologists.

Chapter 2. Swept Source Optical Coherence Tomography Retinal Imaging at 1060nm with Axial Motion Tracking and Dynamic Focus Control using a Variable-Focus Lens

2.1. Introduction

High-resolution visualization of the retinal morphology can assist ophthalmologists to better understand the pathogenesis of retinal diseases. In glaucoma, for example, studies on non-human primates have indicated that morphological changes in the lamina cribrosa may precede the degeneration of retinal ganglion cell (RGC) axons [19]–[21]. Similarly, changes in the density of the photoreceptor mosaic are associated with functional vision loss and retinal degeneration [22], [23].

Optical coherence tomography (OCT) provides cross-sectional images of the retina with exquisite axial resolution, and is commonly used in ophthalmology. In OCT, the axial resolution is determined by the source spectrum, whereas the lateral resolution is determined by the numerical aperture of the sample arm. One trade-off of increasing the lateral resolution is that it reduces the depth of focus, which may not be suitable in clinical situations since a longer depth-of-focus is required to image through the entire thickness of the retina and structures of the optic nerve head (ONH). Therefore, an extended depth-of-focus imaging system capable of maintaining high lateral resolution within the layers of interest is important. Many methods have been proposed in literature to overcome this axial depth limitation. These methods include mechanical motion of the sample arm [24], the addition of focus-modulating elements, such as acousto-optic tunable lenses and Axicon lenses, and adaptive optics [25]–[28]. Multi-beam systems have also been reported [29]. Computational approaches such as interferometric synthetic aperture microscopy (ISAM) have also been successfully used to correct for defocus in post-processing and provide axial focus extension [30], [31].

This chapter describes a novel, auto-focus, high-speed swept-source (SS) OCT imaging system for acquiring high-resolution images of the retina and ONH using a focus stacking method. We incorporated a commercially available variable-focus liquid lens into the optical path that delivered light to the eye. The variable-focus lens is a single-mode deformable optical element that is capable of correcting a wide range of defocus. The variable-focus lens was controlled by a graphics processing unit (GPU)-based processing platform that was used to optimize the focus onto a specific layer, and acquire multiple volumes in rapid succession at different focal depths in the retina. The GPU was also used for removing timing jitter between A-scans from the SS-OCT light source in real-time, which improved the quality of the displayed images. We demonstrate imaging of the entire ONH with high-resolution, from which we can study the morphological changes in the nerve fiber layer and lamina cribrosa due to diseases such as glaucoma. The system is compact, and has a sufficiently large field of view to complement our on-going clinical studies [32], [33].

The remainder of this chapter is organized as follows: we first describe the optical design of our SS-OCT acquisition system. We next describe our custom-written GPU-accelerated retinal tracking and focus optimization algorithm that provided real-time *en face* visualization. The retinal tracking was combined with a simple but rapid segmentation algorithm that provided the metric for layer-specific focusing during optimization, as well as real-time feedback during the optimization process to the user. Lastly, we describe the acquisition and processing steps used to generate a focus-stacked dataset, and present images acquired from human volunteers.

2.2. Methods

We imaged the eyes of human volunteers with their informed consent and with research ethics approval from Simon Fraser University. Imaging was performed using a custom-built 1060 nm swept-source OCT system. The swept-source laser (Axsun technologies, MA) had a center wavelength (λ_c) of 1060 nm and bandwidth ($\Delta\lambda$) of 85 nm, which resulted in a theoretical axial resolution of ~6.2 μm in air. We implemented a ‘double-buffered’ configuration

to increase the A-scan rate from 100 kHz to 200 kHz [34]. The swept-source output was first split 60:40 by a fiber coupler, with the greater percentage power going to the optical delay line (~1 km single-mode fiber) to compensate for the 1.5 dB power loss by the fiber spool. The delayed and original signals were re-combined using a fast optical switch (Nanona Optical Switch, Boston Applied Technologies, Inc., MA) that had a switch time of <60 ns and a maximum cross-talk suppression of 26 dB [35]. The switch output was split 90:10, with 90% of the power going to the OCT system, and the other 10% going to the k-clock calibration signal. The switch was controlled using a 100 kHz, 50% duty cycle TTL signal that was generated using the data acquisition card (National Instruments, TX) and synchronized to the A-scan trigger provided by the swept-source laser. The swept-source laser had a duty cycle of 64%, so the entire spectrum could not be preserved in the buffered output. Instead, we tuned the timing of the TTL signal to include the portion of the spectrum with the greatest intensity. A Fiber-Bragg Grating (FBG, OE Land, Quebec, Canada, λ_c = 985.17 nm, $\Delta\lambda$ = 0.08 nm, reflectivity = 99.16 %) was connected to the other port of the switch to generate the A-scan trigger. This FBG was designed to reflect a narrow wavelength band located near the beginning of the spectrum, outside of the 3 dB bandwidth. Figure 2-1 presents a schematic of the double-buffered source and its connections to the A-scan trigger, k-clock, and OCT system.

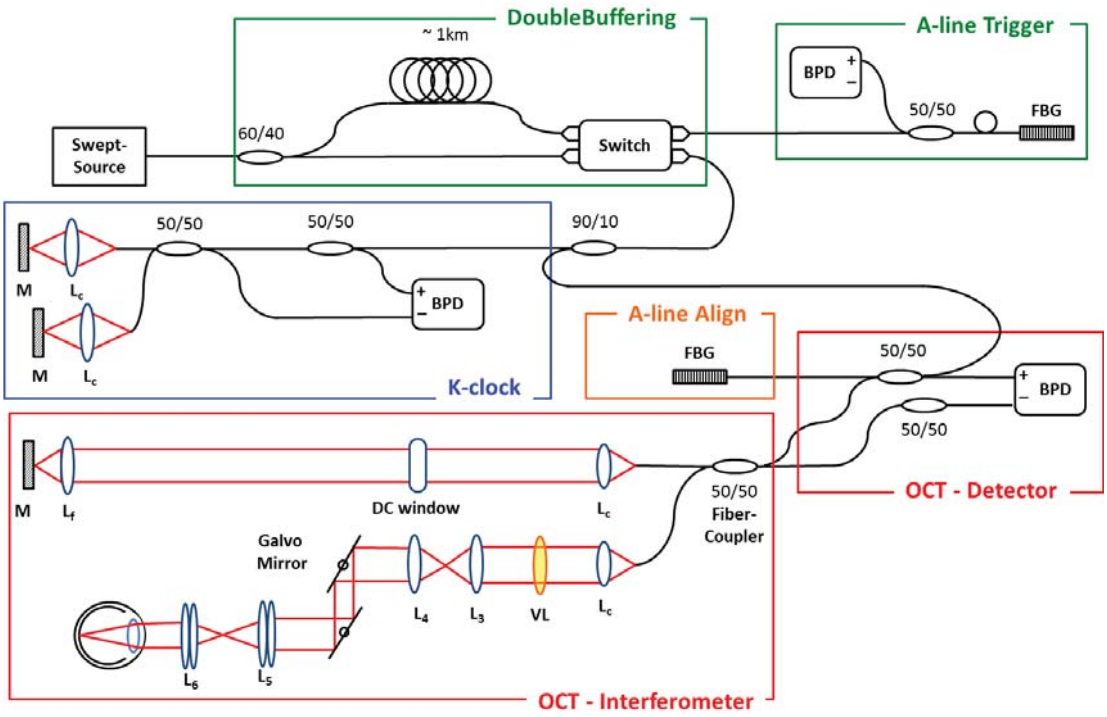

Figure 2-1: Schematic of double-buffered 200 kHz swept-source OCT system, including the A-scan trigger, sampling clock, and OCT system. A variable-focus lens (VL) was included in the sample arm to provide dynamic focus adjustment. The sample arm consisted of two telescopes that relayed the conjugate plane from the variable-focus lens to the scanning mirror and pupil. DC: dispersion compensation; BPD: balanced photo-diode detector; FBG: fiber-Bragg grating; L_c: collimating lens.

The OCT interferometer consisted of three wavelength-flattened couplers in a balanced configuration. A variable-focus lens (VL; ARCTIC 316-AR850, Lyon, France) was added to dynamically adjust the focus of the OCT beam to a user-selected retinal layer. The variable-focus lens had a dynamic range of 18 diopters (-5 D to +13 D), which resulted in an ocular diopter shift of 29 D (-9 D to 20 D). Two telescopes were placed between the VL and ocular pupil to relay the VL, galvanometer-scanning mirrors, and pupil on conjugate planes. The sample arm delivered a 3.0 mm ($1/e^2$ diameter) beam to the pupil, resulting in a calculated ~4.3 μm spot size (FWHM) with ~120 μm depth of focus (calculated as twice the Rayleigh range) at the retina.

2.2.1. Image Acquisition, Segmentation, A-scan Alignment, and Optimization

Two scanning protocols were investigated for the volume acquisition (Figure 2-2). For the conventional approach, we used a raster scan pattern with 80% duty cycle. For each volume, 400×400 A-scans were acquired. This

resulted in an acquisition rate of 1 volume per second. A radial scan approach (Figure 2-2b) was adopted for regions that exhibited centro-symmetry, such as the ONH. In these regions, dense sampling was desirable near the center, whereas sparser-sampling was acceptable near the periphery. For radially acquired data, 180-300 B-scans per volume were acquired evenly spaced in angle, with 600 A-scans per B-scan. Each volume took 0.8-1.2 s to acquire.

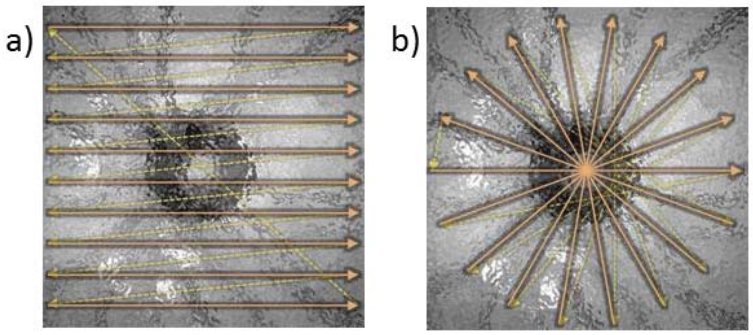

Figure 2-2: Raster (a) and radial scanning (b) protocols. Radial scan was adopted for regions that exhibited radial symmetry, and required denser sampling in the center relative to the periphery.

Our open-sourced GPU-accelerated FD-OCT acquisition code was modified for this project [36]–[38]. For this work, the GPU used was a GeForce GTX Titan (NVIDIA Santa Clara, California) that provided a 1024-pt A-scan processing rate of 4 MHz, which is significantly faster than the data acquisition rate, and thus permitting computational bandwidth for additional processing. The phase instability of the A-scan trigger resulted in undesirable horizontal-line artifacts in the B-scans, which degraded the image quality and potentially interfered with tracking of the brightest layer (Figure 2-3). The artifacts were removed in real-time on the GPU by aligning each A-scan to a reference wavenumber that was provided by an additional Fiber-Bragg Grating (FBG, OE Land, QC, Canada, λ_c = 988.81 nm, $\Delta\lambda$ = 0.05 nm, reflectivity = 93.15 %) in the OCT interferometer (Figure 2-1) [39].

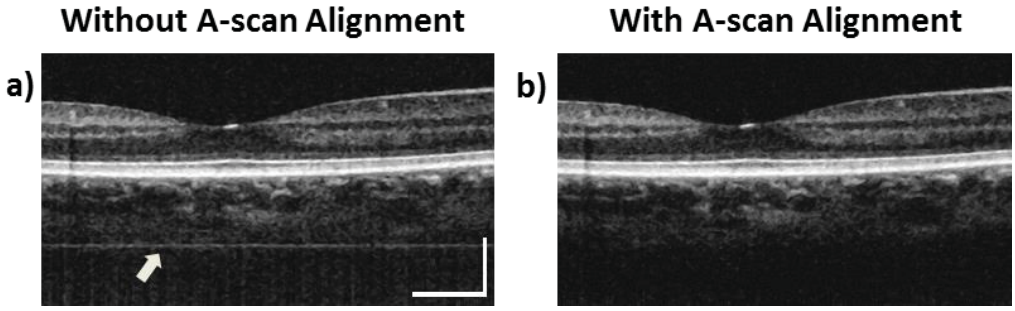

Figure 2-3: DC line artifacts due to A-scan misalignments. a) The DC line artifact is shown with an arrow. b) Alignment of A-scans removed the artifact. Scale bar denotes 300 µm.

A simple segmentation algorithm was implemented in the GPU processing platform to provide real-time axial tracking of the retinal position, which changed due to patient motion, and display of *en face* images from specific layers during acquisition (Figure 2-4). The algorithm tracked the relative position of the brightest layer in the retina to remove the effects of axial motion from the *en face* image. The user selected the thickness of the *en face* layer of interest (indicated by red lines), as well as two reference A-scan positions on the retina (indicated by yellow lines) to be used for tracking (Figure 2-4a). At each reference position, the algorithm determined the pixel with the maximum intensity (indicated by the short blue lines), and used the coordinates to determine the degree of retinal tilt (if present) (Figure 2-4b,c). During acquisition, the user could dynamically adjust the axial offset between the selected layer and brightest layer to display different retinal layers (Figure 2-4d).

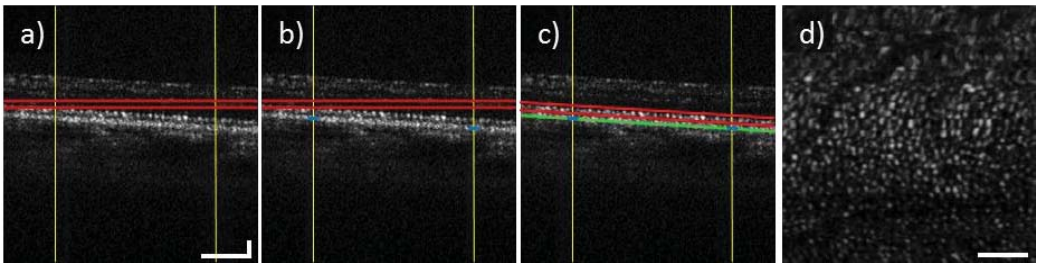

Figure 2-4: Simple segmentation algorithm for real-time axial tracking and *en face* visualization. a) The user manually selected the thickness of *en face* layer (red lines) and two A-scans for segmentation (yellow lines). b) The algorithm detected the maximum-intensity pixel at each location (blue bars). c) The location of the brightest layer in the retina (green line) was interpolated from the two maximum-intensity pixels (blue bars). This location was then used to determine the tilt in the other *en face* layers. d) The *en face* image was generated by summing up the pixels within the two red lines. Scale bar denotes 90 µm.

An optimization algorithm was also developed to provide automated focusing on specific layers. The optimization had a multi-pass approach, starting with a large search range, and then fine-tuning the search range in successive passes. The brightness of the segmented layer was used as the metric for optimization. In the first pass, the optimization algorithm applied 7 different ocular diopter values within a 5-7 D range and recorded the resultant brightness at the specified layer. In the subsequent passes, the algorithm tested a narrower range around the diopter value that gave the maximum intensity in the previous round. For each diopter shift, 10 stationary B-scans/volumes were acquired and used to determine the summed intensity within the selected *en face* region. Thus, we had an optimization rate of 25 Hz per step, and the entire optimization process took approximately 1 sec.

2.2.2. Focus-Stacking Algorithm

High-resolution images of the ONH structures were acquired by merging/blending a set of focus-shifted volumes. First, we automatically optimized the focus at the nerve fiber layer and lamina cribrosa respectively to determine the range of diopter shifts required during acquisition. A set of 3 – 5 volumes were then acquired, with the focus shifted axially between acquisitions. To remove the effects of motion between the datasets, the relative translation between B-scans was assessed using phase correlation. After motion correction, the volumes were then registered using 3D rigid registration in Amira (FEI, OR) followed by 3D non-rigid registration using the Medical Image Registration Toolbox [40], [41]. Lastly, the focal-shifted volumes were blended together using a Gaussian-weighted average, with the Gaussian mask centered upon the most-focused layer for each volume. This resulted in a high resolution volume of the entire ONH [42].

2.3. Results

2.3.1. Results of Real-time tracking and Layer-Specific En face Visualization

Figure 2-5 presents the *en face* views generated using our segmentation and *en face* display code, as presented in real-time during acquisition. The B-scans were also included to show the results of the

segmentation, and the thickness and location of the *en face* layer. In the *en face* image generated from the segmented B-scans, the nerve fiber bundles are clearly visualized. In comparison, without segmentation, artifacts from retinal tilt and axial motion degrade the *en face* image, and the resultant *en face* view is not from a single layer, but is instead a contribution from multiple layers.

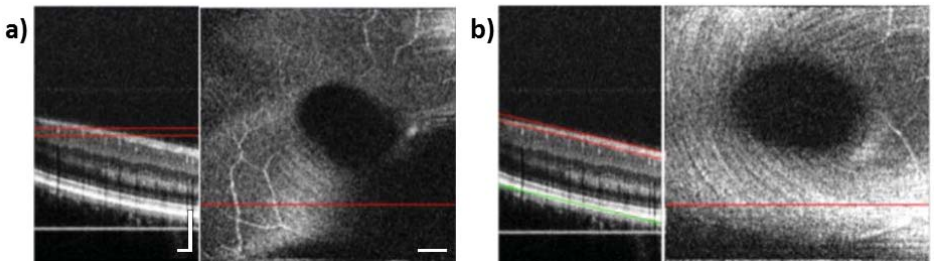

Figure 2-5: Real-time *en face* visualization (a) without and (b) with retinal tracking and anatomically-based segmentation. Scale bar denotes 200 µm.

Figure 2-6 shows representative *en face* images of the nerve fiber layer and the outer plexiform layer, with the focus automatically optimized at the corresponding layer. The high resolution of the system permitted visualization of the nerve fiber bundles in the retinal nerve fiber layer, and the capillary network of the outer plexiform layer with high contrast. Visualization of the circumpapillary nerve fibers in combination with the measurement of retinal nerve fiber layer thickness has potential to improve sensitivity and specificity in detecting glaucoma [43].

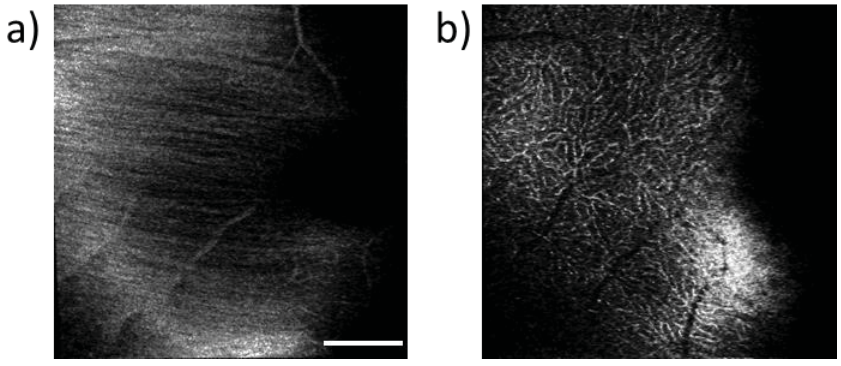

Figure 2-6: *En face* images with focus on a) the nerve fiber layer and b) microvasculature of the outer plexiform layer. Scale bar denotes 400 µm.

Figure 2-7 shows a representative focus-stacked data set acquired at the ONH. In the representative B-scan (Figure 2-7a), we see that the ONH

has high resolution across the entire axial field of view. A representative B-scan from one of the acquired focus-shifted data sets, with the focus set near the lamina cribrosa, is shown for comparison (Figure 2-7b). From the focus-stacked dataset, the nerve fiber layer can be segmented using graph-cut segmentation [44]. A set of Gaussian masks was automatically generated to perform weighted-averaging of the volumes (Figure 2-7d). Figure 2-7e is a stitch of 3 B-scans from Figure 2-7a-c. Depth-resolved images of the lamina cribrosa microarchitecture can also be visualized from the focus-stacked data set, as shown in Figure 2-8.

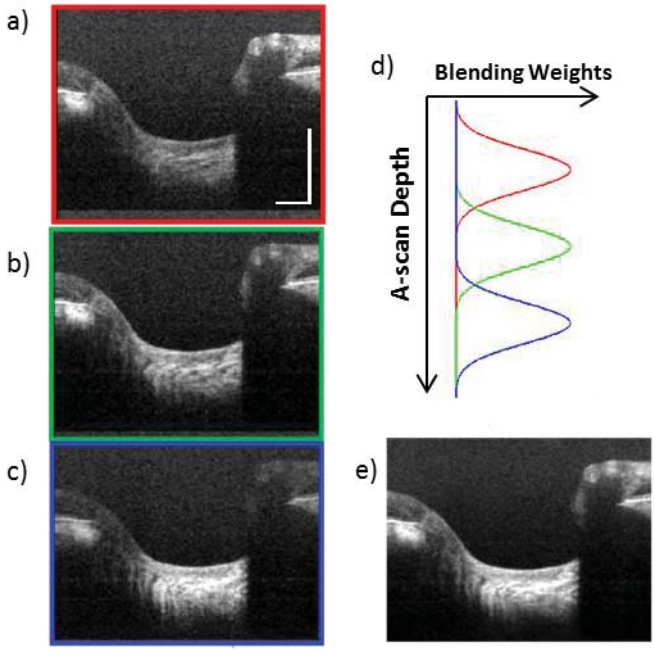

Figure 2-7: Focus-stacking processing and results. a-c) A set of volumes focused at different depths, from the nerve fiber layer (a) to the lamina cribrosa (c) were acquired. d) A set of Gaussian masks are generated to perform weighted-averaging of the volumes. f) Each B-scan from a-c is stitched together. Representative B-scan from the focus-stacked volume shows uniformly high resolution across the entire extent. Scale bar denotes 500 µm.

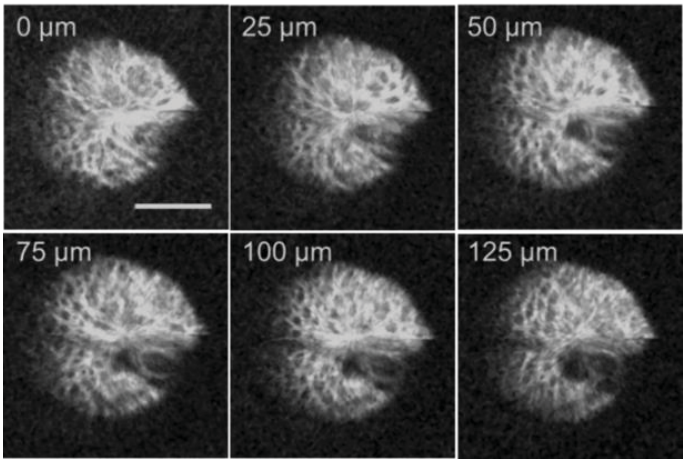

Figure 2-8: Depth-resolved images of lamina cribrosa from a focus-stacked volume, acquired in 25 µm increments from the anterior surface of the lamina cribrosa. Scale bar denotes 500 µm.

2.4. Discussion

We have demonstrated a focus-stacking OCT imaging system with real-time image-based axial retinal tracking and focus optimization. Using the system, we were able to image the ONH with high resolution throughout the axial extent of the structure, from which we could clearly visualize the lamina cribrosa microarchitecture as well as the inner retinal layers. Both of these parameters are important in better identifying factors that precede vision loss in glaucoma [19], [32], [33], [45], [46]. We also demonstrated the system's capability in visualizing the macular microvasculature in the outer plexiform layer and the pattern of nerve fiber bundles emanating from the ONH towards the macula. The ability to visualize and quantify the appearance of nerve fiber bundles traversing the retinal surface has potential as a sensitive early diagnostic biomarker [43], [47], [48].

A key component of our imaging system was the GPU-accelerated real-time retinal tracking and focus optimization algorithm, which allowed real-time *en face* visualization of a user-selected retinal layer for feedback during acquisition. Performing the relevant pre-processing steps in real-time, such as A-scan alignment (correction of A-scan timing jitter) based on the FBG signal, averaging of subsequent frames, etc. permitted relatively simple axial tracking algorithms to work successfully. Axial tracking of the retinal B-scans as they were acquired permitted the visualization of *en face* retinal images with

meaningful correspondence to the cell layer physiology. The real-time image-based axial tracking and segmentation also allowed us to fine-tune our optimization to focus on specific retinal layers instead of optimizing for the brightness along the entire retina. Using our ultrahigh-speed GPU-based processing platform, the focus optimization time was down to approximately 1 sec. The GPU processing results presented in this work are also encouraging for future development of more robust real-time segmentation algorithms. The A-scan processing rate was a factor of 20 higher than the acquisition rate, even with a consumer-grade GPU. With higher-end GPUs and/or multi-GPU configurations, we speculate that segmentation of the intra-retinal layers using techniques such as graph cuts will be realizable in real-time. More sophisticated retinal layer segmentation tools are valuable in cases where edema, drusen, intra-or sub-retinal fluid distort the shape of the retina.

The goal of our system was to build a clinically friendly imaging system that was capable of providing high-resolution information to complement existing retinal imaging systems and glaucoma studies [32], [33]. Thus, although our system has lower resolution than traditional adaptive optics setups, we were able to acquire volumes across a relatively large field of view with sufficiently high resolution to visualize the microarchitecture of the ONH. The inclusion of both high resolution and wide field of view is important for visualizing the pathological changes due to glaucoma in the optic nerve head and in the nerve fiber layer.

We demonstrated human retinal imaging with a variable-focus lens for defocus correction and dynamic focus adjustment. The lateral resolution in the retina could be further improved through the correction of low order aberrations, such as astigmatism, in addition to defocus. Although the pupil diameter of the imaging beam used in this system is larger than that in common commercial OCT instruments in the 830 nm range, the ocular aberrations from the small sample size of subjects imaged (5 people with normal eye health, and mild myopia) did not noticeably detract from the image quality. We anticipate replacing the variable-focus lens element with a more sophisticated adaptive lens to build a compact system that can correct for

higher-order optical aberrations using image-driven optimization [49], [50]. For example, the manufacturer of the variable-focus lens anticipates release of a liquid lens that also provides control of astigmatism. Another tunable lens with defocus and astigmatism correction has also been reported in the literature [51]. Alternatively, the addition of an adaptive lens to correct for higher order aberrations [13] and perform high-resolution *in vivo* retinal imaging would allow for a compact, simple system that would be suitable for translatable for the clinic.

2.5. Conclusion

En face OCT provides important and complementing visualizations of the retina and ONH investigating biomarkers of glaucoma preceding vision loss. We demonstrated the combination of high-performance massively parallel processing of SS-OCT volumetric data for real-time axial tracking and display. In combination with an electrically controllable variable-focus lens, we demonstrated acquisition of focus-stacked OCT volumes with high resolution throughout an extended depth range.

In the next chapter, an advanced deformable lens element called an adaptive lens is introduced for correction of aberrations other than defocus. Extending on the performance of the variable-focus lens, the adaptive lens was capable of deforming to shapes corresponding to higher order Zernike polynomials. However, the adaptive lens had limited stroke for defocus correction, and was inadequate for human retinal imaging alone. The design presented in the next chapter integrates the variable-focus lens with the adaptive lens, delivering a cellular level resolution OCT with a dynamic focus throughout the depth of the retina.

Chapter 3. Swept Source Optical Coherence Tomography at 1060nm with Wavefront Sensorless Adaptive Optics Technique using a Multi-Actuator Adaptive Lens

3.1. Introduction

In the previous chapter, a variable-focus lens was used to acquire high resolution focus stacked images of the retina. However, the lateral resolution was limited by the optical aberrations of the eye. In this chapter, the addition of adaptive optics to obtain higher resolution is investigated.

Adaptive optics concepts have been applied to the advancement of biological imaging and microscopy, for a recent review on this topic please see [52]. In particular, AO has also been very successfully applied to cellular resolution imaging of the retina, enabling visualization of the characteristic mosaic patterns of the outer retinal layers using flood illumination fundus photography [4], scanning laser ophthalmoscopy (SLO) [53], and optical coherence tomography (OCT) [54]–[56]. The maximum attainable lateral resolution on the retina is determined by the diameter of the dilated pupil. Imaging with a narrow diameter beam, about 1 - 2 mm in diameter as with common commercially available retinal diagnostic system, results in a spot size on the retina of nominally 25 μm (diameter). As the diameter of the imaging beam increases, thus increasing the numerical aperture (NA), the optical aberrations in the refractive elements of the eye (cornea and intraocular lens), enlarge and blur the focal spot. Using adaptive optics to correct the wavefront distortions in the eye enables diffraction limited imaging up to the maximum NA of the human eye, NA ~0.25. Despite the high quality of the *in vivo* images attainable with AO, there has been a limited uptake of this technology into clinical ophthalmology.

The exquisite resolution afforded by AO comes at the price of a small field of view and specialized equipment. Recent reports in the literature describe efforts to address the limitations of AO SLO in the clinic [57]. The

typical integration of adaptive optics with an ophthalmic imaging system results in a relatively large and complicated optical setup. The wavefront measurement is commonly performed using a Shack-Hartmann wavefront sensor (SHWFS) placed at an image plane that is optically conjugated to the eye's pupil. The deformable mirror is placed at an optical plane that is conjugated to both the pupil and the SHWFS. Due to the sensitivity of the SHWFS to back reflections, the imaging system is commonly constructed from curved mirrors. In order to reduce the aberrations from the off axis use of mirrors, long focal lengths are used, increasing the size of the system. Out-of-plane configurations have also been proposed to further minimize aberrations [58].

In this chapter, we present a novel lens-based adaptive optics OCT retinal imaging system with significant potential to overcome many of the barriers to integration with a clinical environment. The lens-based AO OCT shares many of the concepts of the retinal imaging system described in Chapter 2, but extended to account for corrections of aberrations of higher order than just defocus. In order to reduce the system size and complexity, we propose the use of a wavefront sensorless adaptive optics (WSAO) algorithm to drive the shape of the wavefront correcting element based on an image quality metric. By eliminating the SHWFS, the WSAO approach is compatible with the lens based optical system described in Chapter 2, and can be readily designed with a simpler and smaller footprint than mirror based systems while maintaining diffraction limited focus. Instead of a deformable mirror, we propose to use a novel transmissive multi-actuator adaptive lens (MAL) capable of correcting aberrations up to 4^{th} radial order Zernike polynomial; the MAL design and operation has been recently described in detail in publication [13]. A benefit of using a transmissive wavefront correcting element is that the adaptive lens can be placed adjacent to a pre-defined pupil plane without the need for an extra optical relay, thus further reducing the footprint of the optical system.

Practical implementation of the WSAO in a clinical environment requires high speed OCT image acquisition and processing capabilities. We

integrated the WSAO algorithm with our comprehensive OCT acquisition and massively parallel processing platform [37]. As in Chapter 2, real-time volumetric display and feature tracking of the OCT cross-sectional retinal images permitted arbitrary user selection of an *en face* depth-plane of interest in the retina (i.e. a particular retinal cell layer) to be used as the input to the merit function for the WSAO aberration correction algorithm. A wavelength swept OCT engine in the 1060 nm wavelength range was selected to reduce the effects of scattering in the ocular anterior chamber, and provide deeper tissue penetration in the retina. The swept source (SS) OCT also provided a combination of rapid line rate and high sensitivity over a large image depth, permitting the full thickness of the retina to be visualized despite the high lateral resolution and short depth of focus.

In the remainder of this chapter, we describe in detail the implementation of a compact lens based MAL-WSAO-SS-OCT, and present retinal images acquired *in vivo* from research volunteers. Widefield images of the retina were used for visualizing the cross-sectional structures of the retinal layers, and for navigating across the retina in relation to anatomical landmarks, such as blood vessels. Narrow field images were used for visualizing the photoreceptor mosaic *en face* at various retinal eccentricities from the fovea. The potential benefits and limitations of the MAL-WSAO-SS-OCT system for clinical retinal imaging are discussed.

3.2. Methods

A picture and a schematic of the MAL-WSAO-SS-OCT system are presented in Figure 3-1. The sub-systems of the OCT engine and the integration with adaptive optics are described individually below.

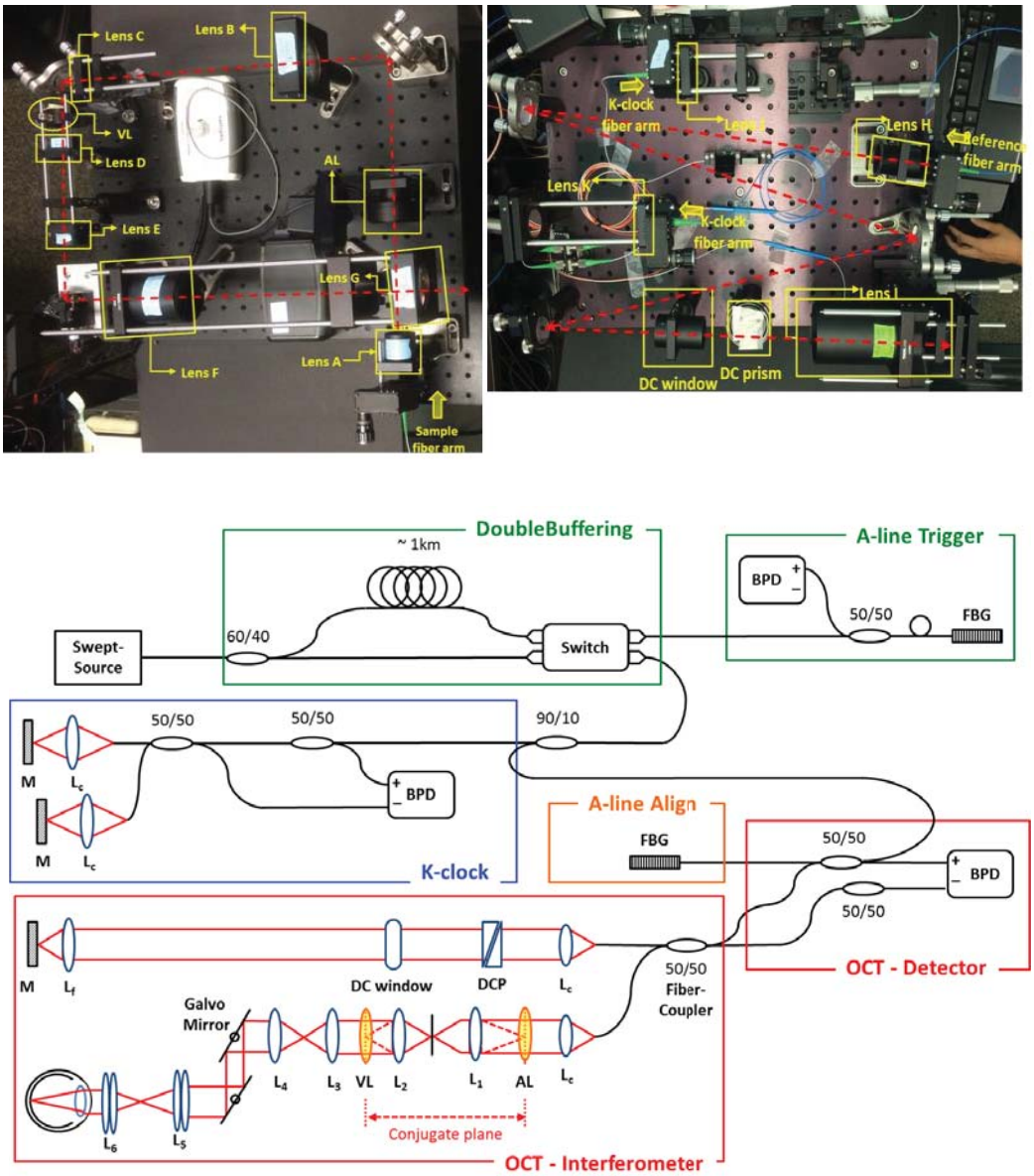

Figure 3-1: a) Picture of the sample arm (left) and the reference arm (right) of the OCT and b) a schematic of the optical system; the schematic is very similar to the variable-focus lens system introduced in the Chapter 2. The main change is that the adaptive lens is added at a conjugate plane of the variable focus lens. DC: dispersion compensation; DCP: DC prisms; BPD: balanced photo-diode detector; FBG: fiber-Bragg grating; L_c: collimating lens.

3.2.1. Swept Source Optical Coherence Tomography engine

The light source used for human retinal imaging was a wavelength swept laser (Axsun Inc, MA) with a 80 nm FWHM spectrum centered at 1060 nm. The line rate of the light source was 100 kHz, with a ~50% duty cycle. In order to increase the imaging speed, we implemented a 'double buffered' approach [35], [59] and a FBG to align A-scans in real time [60]. A fraction of

the source power was sent to a fixed path interferometer, which generated a pixel clock frequency to the Analogue-to-Digital Converter (Alazartech Inc, ATS 9350) in order to sample the OCT data uniformly in wavenumber.

The OCT data was processed and displayed in real time using a custom developed Graphics Processing Unit (GPU) platform that has been previously described [37].The GPU processing was integrated with controls for the deformable lenses, merit function calculation, and real-time z-tracking of the retinal position in software as described in Chapter 2. The user interface permitted dynamic selection of a retinal layer based on the cross-sectional B-scan images, and outputted an *en face* image corresponding to that layer. The image quality of the *en face* image was used for the adaptive optics algorithm, creating a depth resolved metric.

3.2.2. Adaptive optics light delivery to the eye

The sample arm of the OCT system consisted of two deformable optical elements, relay lenses, and galvanometer mounted mirrors to deliver a scanning beam to pupil of the subject being imaged. The MAL was placed at the location of the first lens, which collimated the light from the fiber. This optical plane was conjugated to the variable focus lens via an optical relay. Two additional relays were used to conjugate the optical plane to an XY galvanometer mounted mirror, and then to the subject's pupil. The $1/e^2$ beam diameter at the pupil was calculated to be ~5 mm, corresponding to an estimated focal spot size of 2.1 m ($1/e^2$ Gaussian beam radius) at the retina.

The dual deformable elements created a rudimentary 'woofer-tweeter' adaptive optics system [61]. The purpose of the variable focus lens was to accommodate for the variation in subject's eyes up to approximately -6 diopters without mechanically moving lenses or the pupil plane. Due to the non-linearity and comparatively slow response time of the variable-focus lens, it was adjusted manually to the retinal layer of interest using the cross-sectional OCT images as guidance. The position of the focus within the retina was readily observed as the brightness of the layers changed dynamically as the shape of the lens was changed.

3.2.3. Aberration Correction

The MAL provided the fine tuning of the focus as well as higher order aberration correction. Although the MAL is capable of correcting aberrations up to 4^{th} order Zernike polynomials, we restricted operation to those with highest impacts for a 5 mm beam at the pupil. The modes that we used were defocus, two astigmatisms, two coma, sphere, and two trefoils, corresponding to Zernike modes 4, 3, 5, 6, 7, 10, 8, 9 using the OSA standards [62].The generalized WSAO optimization algorithm we employed was a hill climbing algorithm. For each Zernike mode, the MAL was stepped through a range of coefficient values. At each step, an OCT volume was acquired, and using automated retinal tracking software, an *en face* image corresponding to the retinal layer of interest was extracted. The image quality metric was calculated based on the *en face* image; for OCT the image intensity is a suitable metric [63], although other parameters, such as sharpness, could also be used. Using a hill climbing algorithm, the coefficient that resulted in the brightest image was applied to the MAL, and the next Zernike mode was searched. In this work, we used 10 steps per mode. During optimization, the OCT volume size consisted of 150 x 80 A-scans, which corresponded to an *en face* image acquisition and processing rate of 12.5 frames per second.

The lenses selected for this demonstration of the technology were standard achromatic doublets (Thorlabs Inc. and Edmund Optics, Inc.). The total length of the sample arm was 1.5 m, and was folded to fit on an optical breadboard which was mounted to a slit lamp base (Haag Streit) , providing XYZ translation of the imaging system relative to the subject's eye. The field of view limited by the diameter of the last optical relay was ~7° x 7°.

3.2.4. Human imaging

The performance of the MAL-WSAO-SS-OCT imaging system was demonstrated on research volunteers. Human retinal imaging was performed with informed consent, and with human research ethics approval from Simon Fraser University. Five research volunteers were imaged. The maximum power at the cornea was 750 μW, which is below the safety standard defined by ANSI.

Imaging was performed with the subjects seated at a table with forehead and chin rest; a bite bar was not used during imaging. The operator aligned the imaging beam to the subject's eye under the guidance of an infrared detector. Cross-sectional B-scans of the retina were processed and displayed in real time. During volumetric scans, the *en face* images were also displayed in real time. The operator adjusted the focus to the retinal layer of interest. In the software tool, the corresponding depth region would be selected, and then z-motion would be tracking in the software.

3.3. Results

Conventional OCT was able to scan a large area with almost full depth of focus throughout the retinal layers. Compared to the conventional OCT system, the WSAO OCT system was able to resolve cellular resolution, sacrificing the field of view and the depth of focus.

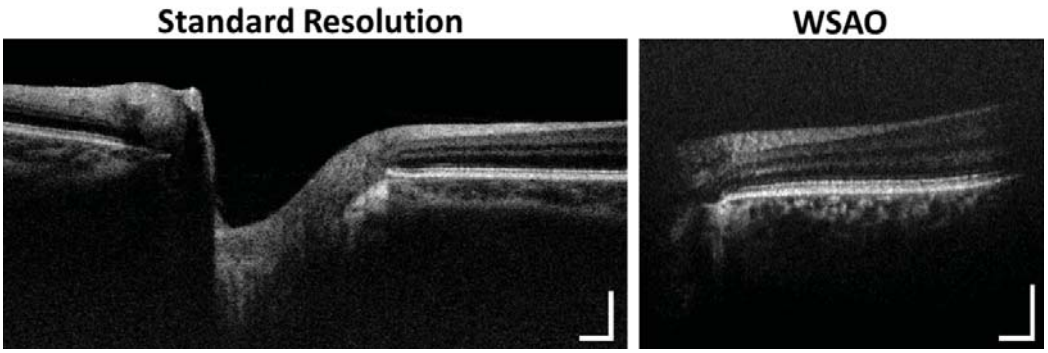

Figure 3-2: Conventional OCT (left) provides wide field images of the retina and optic nerve head. WSAO OCT (right) has a much higher lateral resolution than the conventional OCT, sacrificing the scanning area and the depth of focus. The scale bar represents 250 µm.

Figure 3-3 shows *en face* views of the photoreceptor layers acquired with both the conventional resolution OCT and the WSAO OCT systems. The conventional OCT in Figure 3-3a,b, had a longer depth of focus, extending throughout the retinal layers, but was unable to resolve the photoreceptors as shown in the zoomed-in boxes in Figure 3-3b. On the other hand, the WSAO OCT had a shorter depth of focus which was shifted specifically to the inner segment / outer segment (IS/OS) junction. The aberration-corrected tighter focus at the IS/OS junction allowed visualization of the photoreceptors near the fovea.

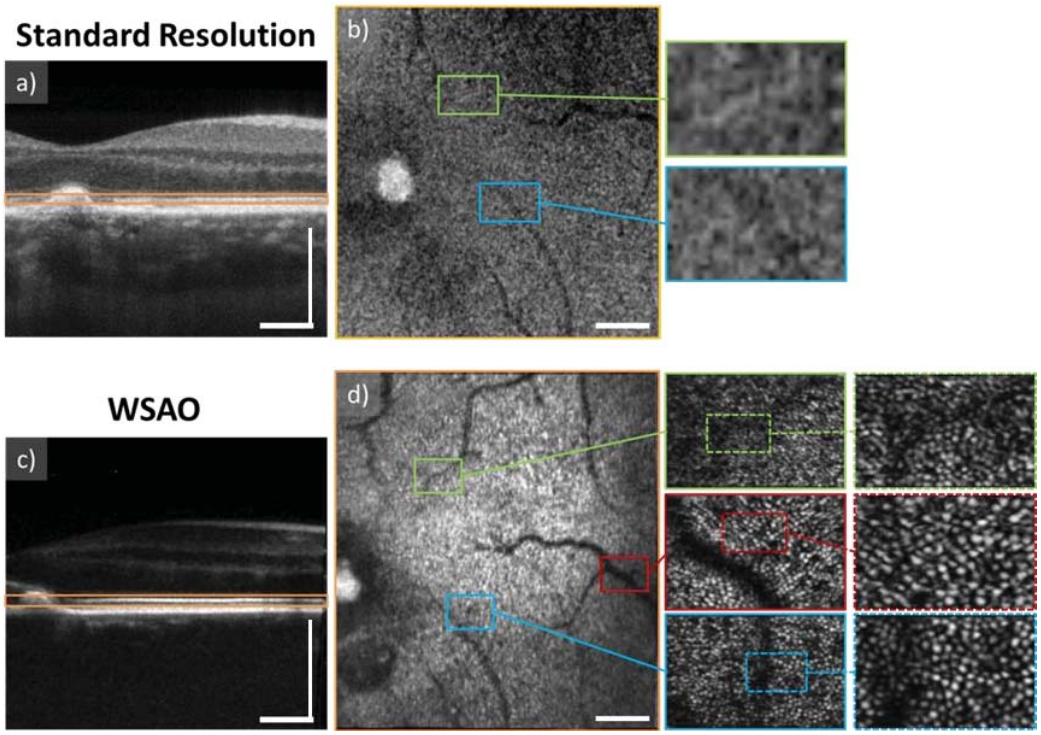

Figure 3-3: A comparison of a conventional OCT (top) and a WSAO OCT (bottom); The imaged location was offset from the fovea with a white blob in the *en face* image representing a drusen; (a) and (c) show flattened B-scans of each system; In the *en face* image of the conventional resolution OCT, (b), the photoreceptors are not resolved whereas the WSAO OCT, (d), was able to resolve the photoreceptors at 3° and 6° eccentricities. The scale bar represents 300 µm.

Wide field images of the human retina are presented in Figure 3-4, with the focus set to the outer retina (photoreceptor layers). The cross-sectional B-scan image of the retina shows the location at the fovea. In the wide field zoomed-in image, the dotted appearance represents photoreceptors, hinting at the lateral resolution of this system. Although the A-scan repetition rate of the laser was 200 kHz, the number of image points was doubled in the fast scan direction by splitting the OCT spectral interferogram [64].

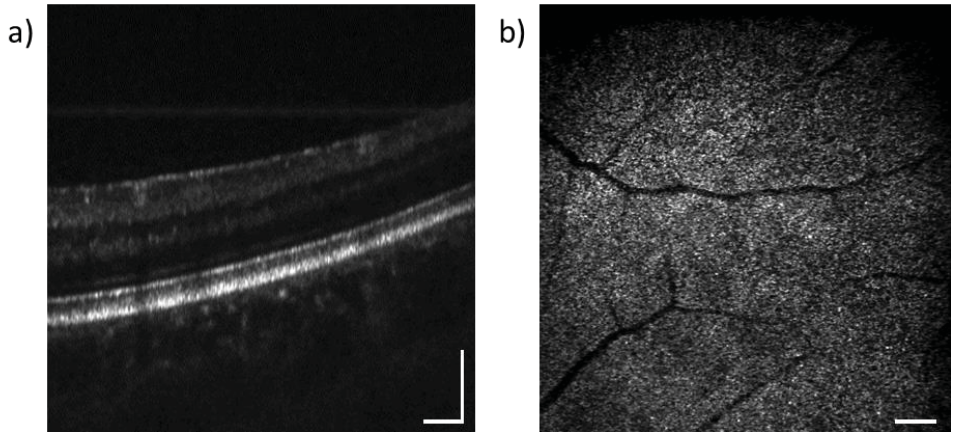

Figure 3-4: Widefield image of normal retina; a) B-scan and b) *en face* of the photoreceptor layer near the fovea. The scale bar represents 200 µm.

The impact of the adaptive optics is demonstrated with the field of view reduced to ~1.35° x 0.68°. Images of human retina acquired at a retinal eccentricity of ~6° are presented in Figure 3-5. These images we acquired by first aligning the subject's fovea approximately with the central field of view of the OCT system (in wide field mode), and then reducing the scan distance. In Figure 3-5a-d, the change in appearance of the photoreceptor layer is demonstrated before and after optimization. Also shown in Figure 3-5e is the recorded values of the image based merit function. The hill climbing algorithm is clearly observed, with the image intensity metric increasing after optimization of each mode. Note that the aberration compensation was performed on a reduced field of view, ~0.68° x 0.34° (200 x100 µm).

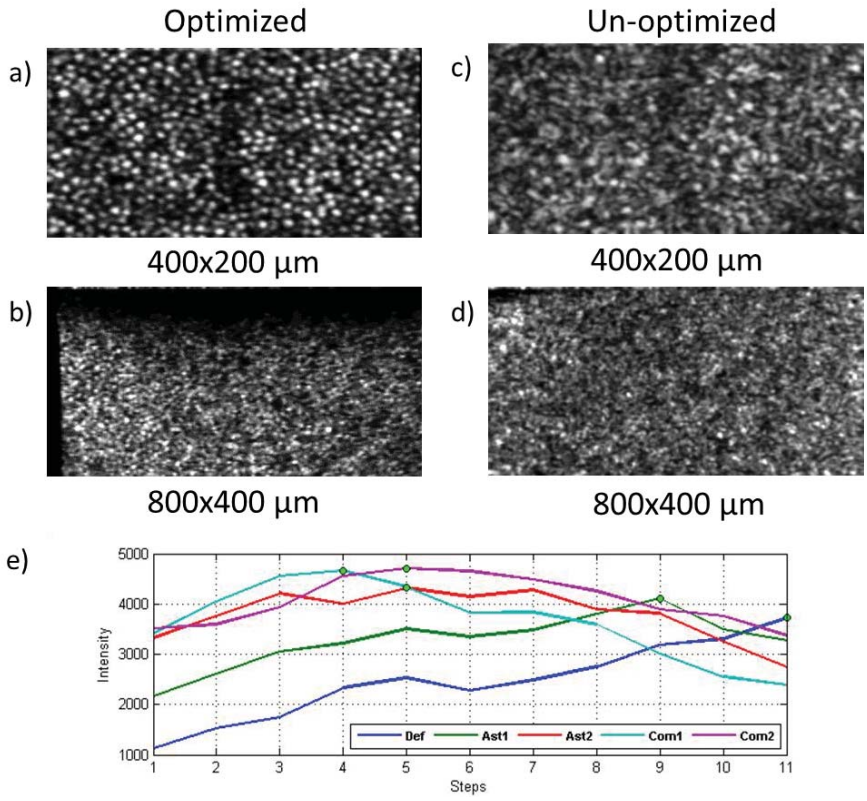

Figure 3-5: Images of the cone photoreceptor mosaic acquired at a retinal eccentricity of 6°. *En face* images on a field of view of 1.35° x 0.68° are presented (a) after and (c) before optimization. The same region is presented in (b) after and (d) before optimization with a 2.71° x 1.35° field of view. The values of the merit function are presented in (d) for each mode during the hill climbing optimization.

A series of photoreceptor images acquired at a same retinal eccentricity (6°) with a different field of view for two different patients are presented in Figure 3-6. At the location, the system was optimized once and varied the galvo scanning range keeping the same number of samples both horizontally and vertically.

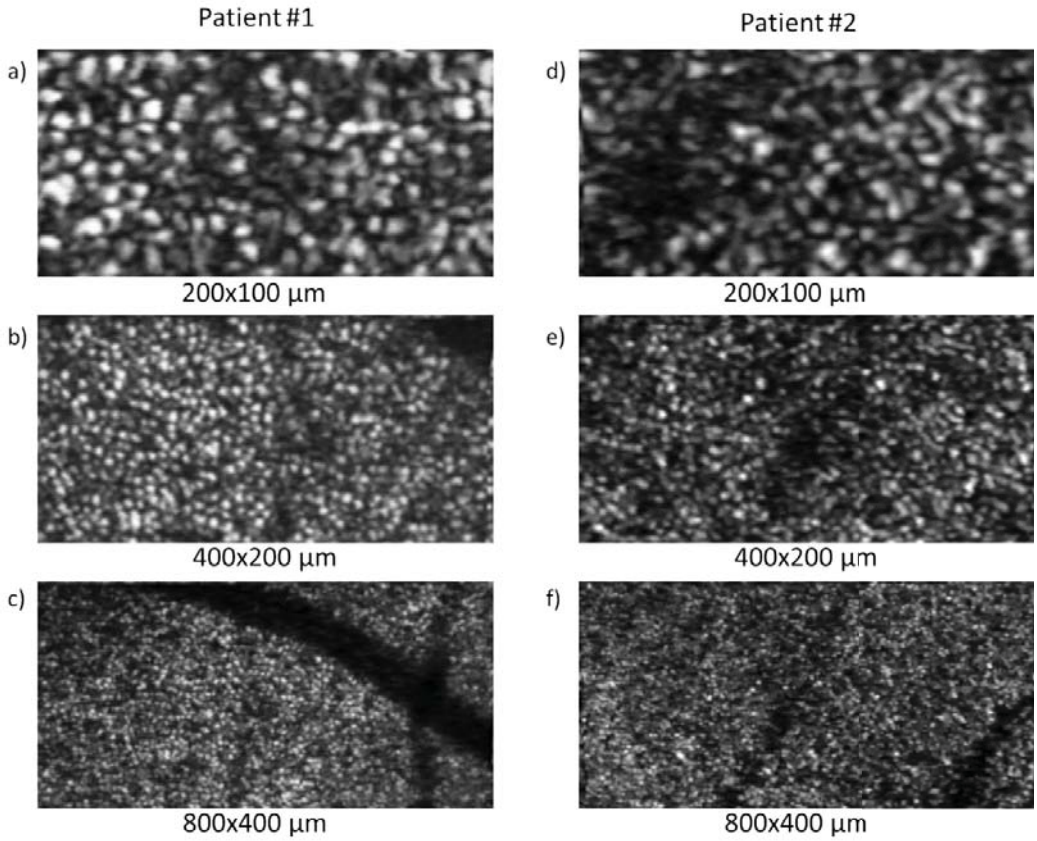

Figure 3-6: Photoreceptor images acquired from the two different patients at similar retinal eccentricity (6°) along the horizontal axis from optic nerve head toward fovea.

In order to demonstrate the versatility of the system, we also acquired images of the nerve fiber layer and the lamina cribrosa, sites on the back of the eye that are associated with glaucoma and other neurodegenerative diseases of the eye. Unlike SHWFS, which treat the retina as a single layer, the WSAO algorithm provides depth resolved aberration correction. For the images in Figure 3-7, the top most retinal layer, corresponding to the retinal nerve fiber bundles, were used for the optimization. In Figure 3-8, the top surface of the lamina cribrosa was used for the optimization.

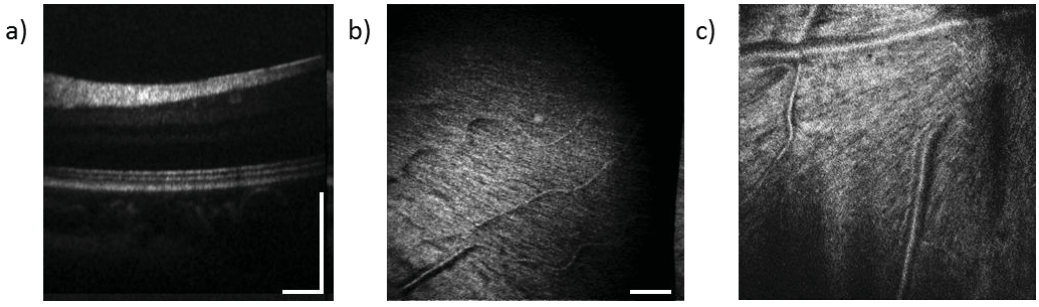

Figure 3-7: WSAO OCT images of the nerve fiber layer at two different locations near the ONH; a) cross-sectional B-scan; b) corresponding *en face* image; and c) another *en face* image at the similar location. The scale bar represents 300 µm.

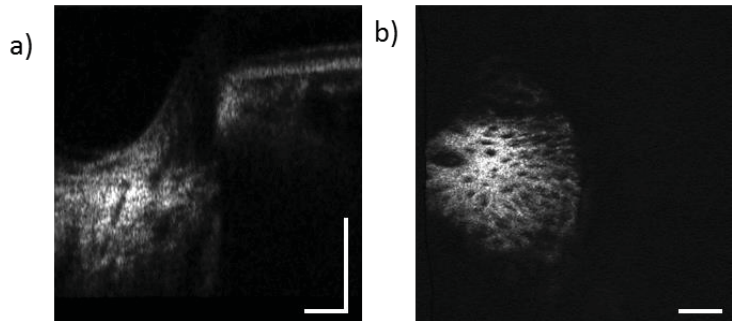

Figure 3-8: WSAO OCT images of the lamina cribrosa at the ONH; a) cross-sectional B-scan; b) corresponding *en face* image. The scale bar represents 300 µm.

3.4. Discussion

Adaptive optics is not currently a part of the clinical standard of care for ophthalmologists. In order for adaptive optics to gain a wider adoption, the system performance needs to be improved in order to provide meaningful information to the clinicians. In our work, we combined adaptive optics for visualization of the photoreceptor mosaic with an OCT system that simultaneously provides images of the retina structure with which the clinicians are already familiar. We have also demonstrated the versatility of the system for imaging nerve fiber bundles and the lamina cribrosa.

A characteristic of OCT is that the axial and lateral resolutions are decoupled; the axial resolution is related to the illumination source spectral bandwidth, while the lateral resolution is dependent on optics of the imaging path. Commercially available ophthalmic OCT systems have a poor lateral resolution because they are designed to image the full thickness of the retina. Reports of conventional WFS AO OCT provide similar quality images of the

outer retinal layer mosaics as the SLO systems [58]. Importantly, the AO-OCT systems also provide cross-sectional images of the retinal layers, permitting the dynamics of photoreceptors to be studied. Although the retina is thicker than the Rayleigh range of the focused beam, the high sensitivity of the OCT system is adequate to visualize the backscattered signal from the inner retina. Unlike the system reported in [58], which are based on spectral domain (SD) OCT systems in the 830 nm range, we developed our imaging system around an SS-OCT operating at 1060 nm.

The selection of operating wavelength used in this report is longer than common AO imaging systems. The obvious disadvantage of the longer wavelength is that the focused spot size at the retina is ~20% larger for an equivalent pupil diameter. However, this is potentially outweighed by the advantages. The longer wavelength is barely visible to the research subject, and is less distracting. The longer wavelength has the advantage of being less sensitive to modest scattering in the cornea and lens, which is common in the eyes of patients at ophthalmic clinics. The lower absorption of the 1060 nm light holds promise for improved visibility of features below the retinal pigment epithelium. Lastly, the lower dispersion of the vitreous humor at 1060 nm is favorable for high resolution OCT imaging with a broad spectrum.

The motivations for using a swept source OCT engine with the WSAO are multi-fold. First, high speed wavelength swept lasers are rapidly becoming available, which is important to reduce imaging time and motion artifact. Newly commercially available light sources operating in the 1060 nm wavelength region are available: for example the Vertical Cavity Surface - Emitting Laser (VCSEL) at several hundred kilohertz [65], and the Fourier Domain Mode Locking (FDML) lasers at up 1.5 MHz. As the technology for high speed SS OCT matures, the combination with the lens based WSAO imaging is complementary. The higher sensitivity of the adaptive optics offsets the loss of sensitivity when imaging rapidly. Additionally, faster imaging reduces the impact of motion artifact on the optimization, and in the appearance of retinal microstructures such as the photoreceptor mosaic. The

wavelength swept lasers have the added benefit that they are less susceptible to so-called phase washout, and permit lateral imaging at faster than the A-scan rate by temporal spectral splitting [64]. Although this technique reduces the axial resolution, the fiber-based interferometer acts as a confocal pinhole and provides some level of optical sectioning. We demonstrated acquisition of *en face* images sampled at twice the A-scan rate of the light source.

The optical configuration of the sample arm delivery optics was entirely lens based aside from the scanning mirrors. The lens based configuration was possible because of the lack of HW-WFS greatly reduced the system sensitivity to back-reflection, and OCT also has low sensitivity to reflected light outside of the coherence length. Our lens based AP sample arm is simple and small in comparison to mirror based AO setups. The foot-print of the prototype MAL-WSAO-SS-OCT sample arm delivery optics was approximately 18” x 24” and was suitable for desk-top operation in a clinical setting, where space is commonly at a premium. With commercial optical design approaches, the size of the optical system could be readily reduced even further. Alternate designs with other deformable element would also likely function well with the WSAO OCT system. Because of the limited defocus correction of the MAL used in this report, we incorporated a second element, the variable focal length lens. Although not strictly a ‘woofer’ as only defocus was corrected, liquid lenses from the same manufacturer that also correct for astigmatism are anticipated to be commercially available in the near term. Another transmissive adaptive lens that can correct astigmatism has also been described in the literature [51]. The versatility of the WSAO OCT algorithm could also be used with a reflective deformable element, for example using a large stroke mirror in place of the MAL and variable focus lens; however, we have not investigated the performance of this configuration.

Another benefit of the lens based sample arm configuration is that it is compatible with a wide field of view in a compact package. The field of view could be further increased through slight changes in configuration from the scanning mirrors to the eye, and use of aspheric lenses. . The field of view that can be imaged with diffraction limited performance is ultimately limited by

the isoplanatic patch of the eye. A wider field of view on the retina with aberration correction could be obtained by mosaicking multiple acquisitions at different retinal eccentricities. The ability to rapidly run the optimization algorithm is essential for these types of applications. Both of the deformable elements used in this report were transmissive.

The WSAO approach to high resolution imaging is flexible. In addition to aberration correction on the outer retina, we demonstrated the ability to correct aberrations on the inner retina directly. Since the image information is used for aberration correction, the anatomical features on which the image-based optimization is performed is always known. This feature also made WSAO OCT imaging of the lamina cribrosa straight forward. In contrast, HW-WFS based approaches rely on a back scattered signal from the whole retina, and simply add a defocus term to the aberration correction in order to shift the focal depth axially through the retina.

The main limitation of the WSAO is the time needed for the algorithm to perform the wavefront correction. With the system presented here, we optimized 5 Zernike modes in ~4 seconds. Replacing the light source in this report with a higher repetition rate laser and the fast-axis galvanometer mounted scanning mirror with a resonant scanner would reduce the convergence time of the adaptive optics algorithm to less than a second without compromising resolution. Another limitation of the WSAO algorithm is that it does not account for accommodation by the intraocular lens. This can be controlled with cycloplegic drugs, and loss of accommodation is a common side effect of mydriasis that is beneficial for WSAO OCT. In this work, we found that the aberration correction image quality was maintained even after patient blinking, and that tear film dynamics were not a major contributor to image aberration for *in vivo* visualization over the course of seconds.

Technical improvements will continue to improve the ease of use of the MAL-WSAO-SS-OCT system. For example, automated blink detection and re-acquisition of the optimization.

3.5. Conclusion

The MAL-WSAO-SS-OCT has the potential to facilitate ophthalmic research to help clinicians better understand changes to the retinal microstructure in disease progressing. Using WSAO techniques enabled a compact lens-based design that is well suited to clinical imaging applicants. The dual adaptive element design and use of a novel transmissive optical element contributed to the performance and compact size of the system. The real time display and z-tracking enabled by the GPU processing platform contribute to the clinical readiness of the system. In the next chapter, future work in preparation for clinical imaging with this system is described, followed by an overall conclusion.

Chapter 4. Future Work

For a clinical system, high-resolution and high-speed optical coherence tomography (OCT) retinal imaging is important to non-invasively visualize the various retinal structures to aid in better understanding of the pathogenesis of vision-robbing diseases. In order to achieve a high-resolution system, we demonstrated a 1060 nm swept-source (SS) OCT integrated with “woofer-tweeter” adaptive optics system using a variable-focus lens and a multi-actuator adaptive lens (MAL).

4.1. Motion rejection

Despite the fact that the system is capable of running at up to 400 kHz (20 volumes per second for the size of 1024 x 200 x 100), the patient’s motion artifact was common during the volume acquisition. To overcome this problem, we streamed multiple (10~30) volumes to disk, which is more than it is required for the volume averaging technique that requires only 3~5 volumes to enhance the SNR. The increase in the number of volumes saved during the acquisition extends the time it requires for the patients to be stable and the time it takes to process the data.

To provide the optimal acquisition and processing time, a motion rejection technique, that tracks a pupil’s movement and position, can be integrated into the system. Using the technique, the system can discard the volumes whenever it detects the eye blink or a movement beyond the certain threshold that cannot be corrected with a post-processing motion registration procedure.

4.2. Bounded-variable least squares

Our current WSAO system uses a pre-generated Zernike mode look-up table using a Matlab function, linear least-square (*lsqlin*). The look-up table consists of 5 Zernike modes including defocus, 1st horizontal and vertical astigmatism, and 1st horizontal and vertical coma. Each mode has ~10 discrete modal coefficient steps that sweep through during the optimization. The fixed number of steps and modes limits the optimality of the WSAO.

Implementing the least-square solver function in real-time with the WSAO C++ based optimization function bounded-variable least squares (BVLS) will allow more freedom in choosing Zernike modes and finer steps to be swept. In addition, the optimal solution can be found using a curve-fitting method after the discrete step search.

4.3. Clinical studies

By providing both retinal cross-sectional images and *en face* cellular resolution, the MAL-WSAO-SS-OCT is well suited to enable a broader investigation of retinal biomarkers of Age-related Macular Degeneration (AMD) such as sub-retinal drusenoid deposits (SDD). The deep tissue penetration and wide field of view of the MAL-WSAO-SS-OCT also make it a versatile tool for imaging in glaucoma studies. The high resolution imaging system also allows the investigation of other types of clinical conditions, such as optic neuropathies [66]. Future application studies with this instrument have the potential to significantly impact the clinical adoption of adaptive optics for high resolution, early stage diagnosis, and monitoring of pathological progression, of diseases causing blindness.

Chapter 5. Conclusion

Various *in vivo* ophthalmic imaging techniques have allowed the identification and early diagnosis of pathological changes in human eyes. Ophthalmic imaging systems such as confocal scanning laser microscopy (cSLO) and conventional fundus camera have high resolution capability but are specialized for *en face* viewing of the retina with a limited retinal layer sectioning ability. Optical coherence tomography (OCT) has allowed visualization of cross-sectional retinal images to diagnose the early stages of retinal diseases such as glaucoma, age-related macular degeneration (AMD), and diabetic retinopathy (RD) [67]. However, when developing an OCT system with high lateral resolution, the corresponding depth of focus is reduced.

To overcome the limitation of the reduced depth of focus of an AO OCT instrument, a deformable liquid lens element, the variable-focus lens (VL), was introduced in Chapter 2. In Chapter 3, wavefront sensorless adaptive optics (WSAO) was introduced along with an additional deformable element, the adaptive lens (AL), to correct higher order aberrations. Integrating both elements, VL and AL, together, we were able to acquire layer-specific cellular level resolution images while compensating for the different defocus and higher order optical aberrations in human eyes.

5.1. Contributions

The double buffered VL system described in Chapter 2 was initially constructed by a former graduate student, Michelle Cua. After joining the project, I made significant technological contributions through stabilization of the k-clock signal that removed vertical line artifacts sporadically occurring in the B-scans. Next, I integrated the fiber-Bragg grating (FBG) to generate a fixed wavenumber reference signal to correct the phase instability in the A-scans. This was important because the instability in the A-scans created horizontal DC artifacts that interrupted the intensity-based layer tracking algorithm. I verified that there existed severe phase instability (up to ±8 wavenumber) and also confirmed that the artifacts were corrected by aligning

the FBG signals together, as described by Poddar et al. [39]. Furthermore, the VL was re-characterized after a change of the lenses of the system configuration. This technical work was essential in order to perform clinical quality retinal imaging. In order to enable human retinal imaging, I assembled a head mount and rebuilt the sample arm of the OCT on top of the slit lamp base (Haag Streit) to readily image the research volunteers. I acquired and processed the numerous numbers of volumes of the retinal structures, such as the nerve fiber bundles, microvasculature of the outer plexiform layer, photoreceptors, and optic nerve head (ONH), which were acquired with both raster and radial scanning methods. I implemented the real-time visualization of the radial scan that provided a useful visual aid of the *en face* image of the retina.

For the WSAO system in Chapter 3, I participated in re-designing and optimizing the optical layout to make the system suitable for clinical imaging in terms of the resolution and the size of the physical layout. I constructed the sample arm from components on top of the slit lamp as shown in Figure 3-1a. I developed the software to generate the Zernike mode look up tables for the AL optimization. As with the VL only system, I acquired a large amount of retinal data from research subjects and processed it with an open source image processing tool, FIJI (ImageJ), and with a pipeline that I built upon the existing MATLAB codes. Furthermore, I fine-tuned the system performance overall, and maximized the optical power at each bulk connector of the optical fibers.

5.2. Potential in Clinical Studies

The compact and high-speed clinically-friendly WSAO OCT holds a great potential for clinical studies by providing cellular resolution *en face* images along with cross-sectional images of the retina. It allows monitoring and measuring structural changes as pathological progression continues such as the thinning of the nerve fiber layer, and loss of the photoreceptors [68]. A limitation of the system developing in this thesis is that the resolution was inadequate to visualize the most central foveal photoreceptors. The reason for this was that the stroke of the prototype adaptive lens limited the imaging

numerical aperture for which aberrations could be corrected. Future developments of the AL will enable higher resolution imaging in human ophthalmic applications. However, even with the current prototype of the AL, there is significant potential for the clinical use of this system in diseases affecting the parafoveal cones, the microvasculature, and nerve fiber bundles.

References

[1] H. W. Babcock, “The possibility of compensating astronomical seeing. Public. of the Astron. Soc. Pac., 65:229-236, 1953.,” *possibility Compens. Astron. seeing*, vol. Public. of, pp. 229–236, 1953.

[2] R. Duffner, *The Adaptive Optics Revolution: A History*. 2009.

[3] J. Rha, R. S. Jonnal, K. E. Thorn, J. Qu, Y. Zhang, and D. T. Miller, “Adaptive optics flood-illumination camera for high speed retinal imaging,” *Opt. Express*, vol. 14, no. 10, p. 4552, May 2006.

[4] D. T. M. junzhong liang, David R. Williams, “Supernormal vision and high-resolution retinal imaging through adaptive optics,” *osa Publ. Vol. 14, Issue 11*, pp. 2284–2892, 1997.

[5] A. Roorda, F. Romero-Borja, W. Donnelly, III, H. Queener, T. Hebert, and M. Campbell, “Adaptive optics scanning laser ophthalmoscopy,” *Opt. Express*, vol. 10, no. 9, p. 405, May 2002.

[6] K. S. K. Wong, Y. Jian, M. Cua, S. Bonora, R. J. Zawadzki, and M. V Sarunic, “In vivo imaging of human photoreceptor mosaic with wavefront sensorless adaptive optics optical coherence tomography.,” *Biomed. Opt. Express*, vol. 6, no. 2, pp. 580–90, Feb. 2015.

[7] F. A. V.-D. and N. Doble, *Topics in Adaptive Optics*. InTech, 2012.

[8] J. A. Kubby, *Adaptive Optics for Biological Imaging*. 2013.

[9] von F. Zernike, “Beugungstheorie des schneidenver-fahrens und seiner verbesserten form, der phasenkontrastmethode,” *Physica*, vol. 1, no. 7–12, pp. 689–704, May 1934.

[10] M. Born and E. Wolf, “Principle of optics,” *Pergamon Press 6th edn.*, 1983.

[11] M. J. Booth, “Adaptive optics in microscopy.,” *Philos. Trans. A. Math. Phys. Eng. Sci.*, vol. 365, no. 1861, pp. 2829–43, Dec. 2007.

[12] J. C. Dainty, A. V. Koryabin, and A. V. Kudryashov, “Low-Order Adaptive Deformable Mirror,” *Appl. Opt.*, vol. 37, no. 21, p. 4663, Jul. 1998.

[13] S. Bonora, Y. Jian, P. Zhang, A. Zam, E. N. Pugh, R. J. Zawadzki, and M. V. Sarunic, “Wavefront correction and high-resolution in vivo OCT imaging with an objective integrated multi-actuator adaptive lens,” *Opt. Express*, vol. 23, no. 17, p. 21931, Aug. 2015.

[14] P. Artal, S. Marcos, R. Navarro, and D. R. Williams, “Odd aberrations and double-pass measurements of retinal image quality.,” *J. Opt. Soc. Am. A. Opt. Image Sci. Vis.*, vol. 12, no. 2, pp. 195–201, Feb. 1995.

[15] M. Booth, “Wave front sensor-less adaptive optics: a model-based approach using sphere packings.,” *Opt. Express*, vol. 14, no. 4, pp. 1339–52, Feb. 2006.

[16] A. J. Wright, D. Burns, B. A. Patterson, S. P. Poland, G. J. Valentine, and J. M. Girkin, “Exploration of the optimisation algorithms used in the implementation of adaptive optics in confocal and multiphoton microscopy.,” *Microsc. Res. Tech.*, vol. 67, no. 1, pp. 36–44, May 2005.

[17] D. Debarre, M. J. Booth, and T. Wilson, “Image based adaptive optics through optimisation of low spatial frequencies,” *Opt. Express*, vol. 15, no. 13, p. 8176, Jun. 2007.

[18] Y. Jian, J. Xu, M. A. Gradowski, S. Bonora, R. J. Zawadzki, and M. V Sarunic, “Wavefront sensorless adaptive optics optical coherence tomography for in vivo retinal imaging in mice.,” *Biomed. Opt. Express*, vol. 5, no. 2, pp. 547–59, Feb. 2014.

[19] A. J. Bellaza, C. J. Rintalan, H. W. Thompson, J. C. Downs, R. T. Hart, and C. F. Burgoyne, “Deformation of the Lamina Cribrosa and Anterior Scleral Canal Wall in Early Experimental Glaucoma,” *Invest. Ophthalmol. Vis. Sci.*, vol. 44, no. 2, pp. 623–637, Feb. 2003.

[20] J. Crawford Downs, M. D. Roberts, and I. a Sigal, “Glaucomatous cupping of the lamina cribrosa: a review of the evidence for active progressive remodeling as a mechanism.,” *Exp. Eye Res.*, vol. 93, no. 2, pp. 133–40, Aug. 2011.

[21] B. Wang, J. E. Nevins, Z. Nadler, G. Wollstein, H. Ishikawa, R. a Bilonick, L. Kagemann, I. a Sigal, I. Grulkowski, J. J. Liu, M. Kraus, C. D. Lu, J. Hornegger, J. G. Fujimoto, and J. S. Schuman, “In vivo lamina cribrosa micro-architecture in healthy and glaucomatous eyes as assessed by optical coherence tomography.,” *Invest. Ophthalmol. Vis. Sci.*, vol. 54, no. 13, pp. 8270–4, Dec. 2013.

[22] C. A. Curcio, “Photoreceptor topography in ageing and age-related maculopathy.,” *Eye (Lond).*, vol. 15, no. Pt 3, pp. 376–83, Jun. 2001.

[23] S. S. Choi, N. Doble, J. L. Hardy, S. M. Jones, J. L. Keltner, S. S. Olivier, and J. S. Werner, “In vivo imaging of the photoreceptor mosaic in retinal dystrophies and correlations with visual function.,” *Invest. Ophthalmol. Vis. Sci.*, vol. 47, no. 5, pp. 2080–92, May 2006.

[24] M. Pircher, E. Götzinger, and C. K. Hitzenberger, “Dynamic focus in optical coherence tomography for retinal imaging.,” *J. Biomed. Opt.*, vol. 11, no. 5, p. 054013, 2006.

[25] I. Grulkowski, K. Szulzycki, and M. Wojtkowski, “Microscopic OCT imaging with focus extension by ultrahigh-speed acousto-optic tunable lens and stroboscopic illumination,” *Opt. Express*, vol. 22, no. 26, p. 31746, Dec. 2014.

[26] R. A. Leitgeb, M. Villiger, A. H. Bachmann, L. Steinmann, and T. Lasser, “Extended focus depth for Fourier domain optical coherence microscopy,” *Opt. Lett.*, vol. 31, no. 16, p. 2450, 2006.

[27] C. Blatter, B. Grajciar, C. M. Eigenwillig, W. Wieser, B. R. Biedermann, R. Huber, and R. A. Leitgeb, “Extended focus high-speed swept source OCT with self-reconstructive illumination.,” *Opt. Express*, vol. 19, no. 13, pp. 12141–55, Jun. 2011.

[28] K. Sasaki, K. Kurokawa, S. Makita, and Y. Yasuno, “Extended depth of focus adaptive optics spectral domain optical coherence tomography.,” *Biomed. Opt. Express*, vol. 3, no. 10, pp. 2353–70, Oct. 2012.

[29] J. Holmes, “Theory and applications of multi-beam OCT,” *SPIE Proc.*, vol. 7139, p. 713908, 2008.

[30] S. G. Adie, B. W. Graf, A. Ahmad, P. S. Carney, and S. A. Boppart, “Computational adaptive optics for broadband optical interferometric tomography of biological tissue.,” *Proc. Natl. Acad. Sci. U. S. A.*, vol. 109, no. 19, pp. 7175–80, May 2012.

[31] Y.-Z. Liu, N. D. Shemonski, S. G. Adie, A. Ahmad, A. J. Bower, P. S. Carney, and S. A. Boppart, “Computed optical interferometric tomography for high-speed volumetric cellular imaging.,” *Biomed. Opt. Express*, vol. 5, no. 9, pp. 2988–3000, Sep. 2014.

[32] S. Lee, S. X. Han, M. Young, M. F. Beg, M. V Sarunic, and P. J. Mackenzie, “Optic nerve head and peripapillary morphometrics in myopic glaucoma.,” *Invest. Ophthalmol. Vis. Sci.*, vol. 55, no. 7, pp. 4378–93, Jul. 2014.

[33] M. Young, S. Lee, M. Rateb, M. F. Beg, M. V Sarunic, and P. J. Mackenzie, “Comparison of the clinical disc margin seen in stereo disc photographs with neural canal opening seen in optical coherence tomography images.,” *J. Glaucoma*, vol. 23, no. 6, pp. 360–7, Aug. 2014.

[34] B. Potsaid, B. Baumann, D. Huang, S. Barry, A. E. Cable, J. S. Schuman, J. S. Duker, and J. G. Fujimoto, “Ultrahigh speed 1050nm swept source / Fourier domain OCT retinal and anterior segment imaging at 100,000 to 400,000 axial scans per second,” vol. 18, no. 19, pp. 20029–20048, 2011.

[35] A.-H. Dhalla, K. Shia, and J. A. Izatt, “Efficient sweep buffering in swept source optical coherence tomography using a fast optical switch.,” *Biomed. Opt. Express*, vol. 3, no. 12, pp. 3054–66, Dec. 2012.

[36] Y. Jian, K. Wong, and M. V. Sarunic, “GPU accelerated OCT processing at megahertz axial scan rate and high resolution video rate volumetric rendering,” in *SPIE BiOS*, 2013, p. 85710Z.

[37] Y. Jian, K. Wong, and M. V Sarunic, “Graphics processing unit accelerated optical coherence tomography processing at megahertz axial scan rate and high resolution video rate volumetric rendering.,” *J. Biomed. Opt.*, vol. 18, no. 2, p. 26002, Feb. 2013.

[38] J. Xu, K. Wong, Y. Jian, and M. V Sarunic, “Real-time acquisition and display of flow contrast using speckle variance optical coherence tomography in a graphics processing unit.,” *J. Biomed. Opt.*, vol. 19, no. 2, p. 026001, Feb. 2014.

[39] R. Poddar, P. Raju, D. E. Cortés, J. S. Werner, M. J. Mannis, and R. J. Zawadzki, “Three-dimensional anterior segment imaging in patients with type 1 Boston Keratoprosthesis with switchable full depth range swept source optical coherence tomography.,” *J. Biomed. Opt.*, vol. 18, no. 8, p. 86002, Aug. 2013.

[40] E. Gibson, M. Young, M. V Sarunic, and M. F. Beg, “Optic nerve head registration via hemispherical surface and volume registration.,” *IEEE Trans. Biomed. Eng.*, vol. 57, no. 10, pp. 2592–5, Oct. 2010.

[41] S. Lee, E. Lebed, M. V Sarunic, and M. F. Beg, “Exact surface registration of retinal surfaces from 3-d optical coherence tomography images.,” *IEEE Trans. Biomed. Eng.*, vol. 62, no. 2, pp. 609–17, Feb. 2015.

[42] M. Cua, E. Lin, L. Lee, X. Sheng, K. S. K. Wong, G. F. Tibbits, M. F. Beg, and M. V Sarunic, “Morphological phenotyping of mouse hearts using optical coherence tomography.,” *J. Biomed. Opt.*, vol. 19, no. 11, p. 116007, Jan. 2014.

[43] D. C. Hood, M. F. Chen, D. Lee, B. Epstein, P. Alhadeff, R. B. Rosen, R. Ritch, A. Dubra, and T. Y. P. Chui, “Confocal Adaptive Optics Imaging of Peripapillary Nerve Fiber Bundles: Implications for Glaucomatous Damage Seen on Circumpapillary OCT Scans.,” *Transl. Vis. Sci. Technol.*, vol. 4, no. 2, p. 12, Apr. 2015.

[44] S. Lee, N. Fallah, F. Forooghian, A. Ko, K. Pakzad-Vaezi, A. B. Merkur, A. W. Kirker, D. A. Albiani, M. Young, M. V Sarunic, and M. F. Beg, “Comparative analysis of repeatability of manual and automated choroidal thickness measurements in nonneovascular age-related macular degeneration.,” *Invest. Ophthalmol. Vis. Sci.*, vol. 54, no. 4, pp. 2864–71, Apr. 2013.

[45] T.-W. Kim, L. Kagemann, M. J. a Girard, N. G. Strouthidis, K. R. Sung, C. K. Leung, J. S. Schuman, and G. Wollstein, “Imaging of the lamina cribrosa in glaucoma: perspectives of pathogenesis and clinical applications.,” *Curr. Eye Res.*, vol. 38, no. 9, pp. 903–9, Sep. 2013.

[46] C. W. Spraul, G. E. Lang, G. K. Lang, and H. E. Grossniklaus, “Morphometric changes of the choriocapillaris and the choroidal vasculature in eyes with advanced glaucomatous changes,” *Vision Res.*, vol. 42, no. 7, pp. 923–932, Mar. 2002.

[47] M. F. Chen, T. Y. P. Chui, P. Alhadeff, R. B. Rosen, R. Ritch, A. Dubra, and D. C. Hood, “Adaptive Optics Imaging of Healthy and Abnormal Regions of Retinal Nerve Fiber Bundles of Patients With Glaucoma,” *Invest. Ophthalmol. Vis. Sci.*, vol. 56, no. 1, pp. 674–681, Jan. 2015.

[48] C. K. Leung, C. Y. L. Cheung, R. N. Weinreb, K. Qiu, S. Liu, H. Li, G. Xu, N. Fan, C. P. Pang, K. K. Tse, and D. S. C. Lam, “Evaluation of retinal nerve fiber layer progression in glaucoma: a study on optical coherence tomography guided progression analysis.,” *Invest. Ophthalmol. Vis. Sci.*, vol. 51, no. 1, pp. 217–22, Jan. 2010.

[49] Y. Jian, J. Xu, M. A. Gradowski, S. Bonora, R. J. Zawadzki, and M. V Sarunic, “Wavefront sensorless adaptive optics optical coherence tomography for in vivo retinal imaging in mice.,” *Biomed. Opt. Express*, vol. 5, no. 2, pp. 547–59, Feb. 2014.

[50] K. S. K. Wong, Y. Jian, M. Cua, S. Bonora, R. J. Zawadzki, and M. V. Sarunic, “In vivo imaging of human photoreceptor mosaic with wavefront sensorless adaptive optics optical coherence tomography,” *Biomed. Opt. Express*, vol. 6, no. 2, p. 580, Jan. 2015.

[51] P. Liebetraut, S. Petsch, J. Liebeskind, and H. Zappe, “Elastomeric lenses with tunable astigmatism,” *Light Sci. Appl.*, vol. 2, no. 9, p. e98, Sep. 2013.

[52] M. J. Booth, “Adaptive optical microscopy: the ongoing quest for a perfect image,” *Light Sci. Appl.*, vol. 3, no. 4, p. e165, Apr. 2014.

[53] A. Roorda, “Applications of adaptive optics scanning laser ophthalmoscopy.,” *Optom. Vis. Sci.*, vol. 87, no. 4, pp. 260–8, Apr. 2010.

[54] R. J. Zawadzki, S. M. Jones, S. S. Olivier, M. Zhao, B. A. Bower, J. A. Izatt, S. Choi, S. Laut, and J. S. Werner, “Adaptive-optics optical coherence tomography for high-resolution and high-speed 3D retinal in vivo imaging.,” *Opt. Express*, vol. 13, no. 21, pp. 8532–8546, Oct. 2005.

[55] Y. Jian, R. J. Zawadzki, and M. V Sarunic, “Adaptive optics optical coherence tomography for in vivo mouse retinal imaging.,” *J. Biomed. Opt.*, vol. 18, no. 5, p. 56007, May 2013.

[56] O. P. Kocaoglu, T. L. Turner, Z. Liu, and D. T. Miller, “Adaptive optics optical coherence tomography at 1 MHz.,” *Biomed. Opt. Express*, vol. 5, no. 12, pp. 4186–200, Dec. 2014.

[57] J. Zhang, Q. Yang, K. Saito, K. Nozato, D. R. Williams, and E. A. Rossi, “An adaptive optics imaging system designed for clinical use.,” *Biomed. Opt. Express*, vol. 6, no. 6, pp. 2120–37, Jun. 2015.

[58] S.-H. Lee, J. S. Werner, and R. J. Zawadzki, “Improved visualization of outer retinal morphology with aberration cancelling reflective optical design for adaptive optics - optical coherence tomography.,” *Biomed. Opt. Express*, vol. 4, no. 11, pp. 2508–17, Jan. 2013.

[59] R. Huber, D. C. Adler, and J. G. Fujimoto, “Buffered Fourier domain mode locking: unidirectional swept laser sources for optical coherence tomography imaging at 370,000 lines/s,” *Opt. Lett.*, vol. 31, no. 20, p. 2975, Oct. 2006.

[60] R. Poddar, D. Y. Kim, J. S. Werner, and R. J. Zawadzki, “In vivo imaging of human vasculature in the chorioretinal complex using phase-variance contrast method with phase-stabilized 1-μm swept-source optical coherence tomography.,” *J. Biomed. Opt.*, vol. 19, no. 12, p. 126010, Dec. 2014.

[61] W. Zou, X. Qi, and S. A. Burns, “Woofer-tweeter adaptive optics scanning laser ophthalmoscopic imaging based on Lagrange-multiplier damped least-squares algorithm.,” *Biomed. Opt. Express*, vol. 2, no. 7, pp. 1986–2004, Jul. 2011.

[62] L. N. Thibos, R. A. Applegate, J. T. Schwiegerling, and R. Webb, “Standards for reporting the optical aberrations of eyes.,” *J. Refract. Surg.*, vol. 18, no. 5, pp. S652–60, Jan. .

[63] Y. N. Sulai and A. Dubra, “Non-common path aberration correction in an adaptive optics scanning ophthalmoscope.,” *Biomed. Opt. Express*, vol. 5, no. 9, pp. 3059–73, Sep. 2014.

[64] L. Ginner, C. Blatter, D. Fechtig, T. Schmoll, M. Gröschl, and R. Leitgeb, “Wide-Field OCT Angiography at 400 KHz Utilizing Spectral Splitting,” *Photonics*, vol. 1, no. 4, pp. 369–379, Oct. 2014.

[65] I. Grulkowski, J. J. Liu, B. Potsaid, V. Jayaraman, J. Jiang, J. G. Fujimoto, and A. E. Cable, “High-precision, high-accuracy ultralong-range swept-source optical coherence tomography using vertical cavity surface emitting laser light source.,” *Opt. Lett.*, vol. 38, no. 5, pp. 673–5, Mar. 2013.

[66] S. S. Choi, R. J. Zawadzki, J. L. Keltner, and J. S. Werner, “Changes in cellular structures revealed by ultra-high resolution retinal imaging in

optic neuropathies.," *Invest. Ophthalmol. Vis. Sci.*, vol. 49, no. 5, pp. 2103–19, May 2008.

[67] M. Wojtkowski, "High-speed optical coherence tomography: basics and applications.," *Appl. Opt.*, vol. 49, no. 16, pp. D30–61, Jun. 2010.

[68] D. T. Miller, O. P. Kocaoglu, Q. Wang, and S. Lee, "Adaptive optics and the eye (super resolution OCT).," *Eye (Lond).*, vol. 25, no. 3, pp. 321–30, Mar. 2011.